Montanuniversität Leoben

Sputtered polymeric hydrogenated amorphous carbon thin films for temporary medical implants

Gesputterte polymerartige amorphe hydrogenisierte Kohlenstoffschichten für temporäre medizinische Implantate

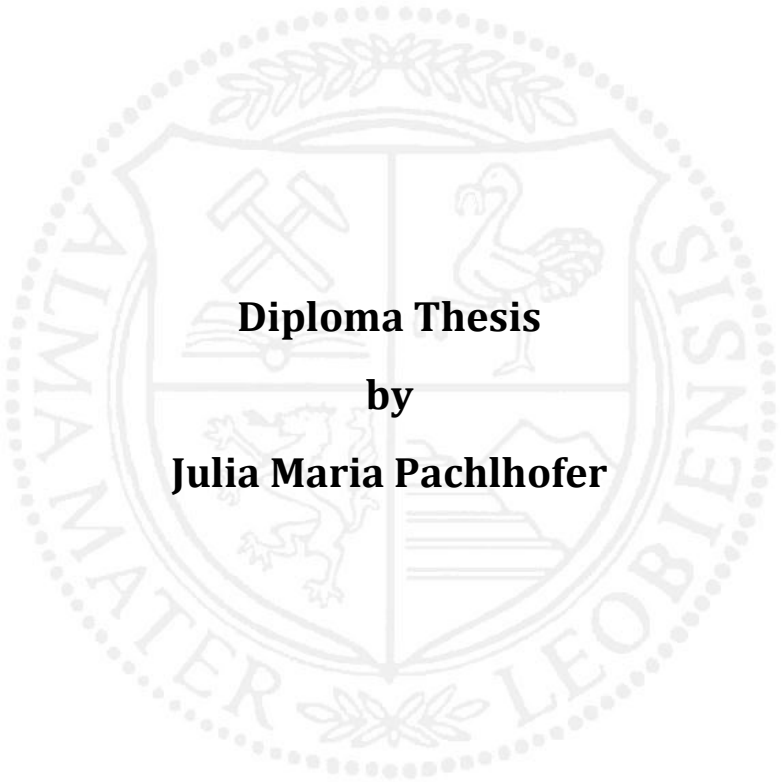

Diploma Thesis

by

Julia Maria Pachlhofer

This work has been carried out at the Chair of Functional Materials and Materials Systems at the Department of Physical Metallurgy and Materials Testing, Montanuniversität Leoben, Austria.

Leoben, March 2013

Affidavit

I declare in lieu of oath that I did the diploma thesis by myself using only literature cited in this work.

Leoben, March 2013

Acknowledgement

I would like to express my sincere gratitude to Univ.-Prof. Christian Mitterer for providing me with the opportunity of writing this interesting thesis at the Chair of Functional Materials and Materials Systems, for his supervision, the patience and the confidence he placed in me.

I am very grateful to Oliver for his patience and great support while supervising me at writing this thesis.

Many thanks go to all members of the thin film group for the great support whenever needed and the pleasurable working atmosphere. A special thanks goes to Sabrina and Karl-Heinz for all the troubles with our exhausting ladies Esmeralda and Mutti.

I would like to thank Hilde for helping with all bureaucratic problems during my work at the department.

I am grateful to Mr. Frans Munnik for the Helmholtz-Centre Dresden-Rossendorf for carrying out the ERDA measurements. Furthermore, I would like to thank Ass.Prof. Thomas Grießer and Matthias Edler for carrying out and analysing the XPS measurements.

A special thanks goes to all my friends I found in Leoben for the great times we had, have and will have, especially to “meine Mädls” Astrid, Leni, Marion and Tamara, who always have a sympathetic ear for me and on whom I can rely.

Last but not least … möchte ich mich bei meiner Familie bedanken. Ohne deren moralische sowie finanzielle Unterstützung wäre dieses Studium nicht möglich gewesen.

Table of Contents

ABBREVIATIONS

a-C	…	amorphous carbon
a-C:H	…	hydrogenated amorphous carbon
Ar	…	argon
Ar^+	…	argon ions
C	…	carbon
C_2H_2	…	acetylene
$(CH_2)_n$	…	methylene
CAE	…	Constant Analyzer Energy
CBMS	…	Conventional Balanced Magnetron Sputtering
D	…	disordered
DC	…	Direct Current
DLC	…	diamond-like carbon
ERDA	…	Elastic Recoil Detection Analysis
FIB	…	Focused Ion Beam
FWHM (G)	…	full width at half maximum of the G-band
G	…	graphite
H	…	hydrogen
I_D/I_G	…	Intensity ratio
I_m	…	current at magnetron
I_s	…	current at substrate holder
N	…	nitrogen
O	…	oxygen
PECVD	…	Plasma-Enhanced Chemical Vapour Deposition
P_m	…	power at magnetron
PVD	…	Physical Vapour Deposition
RBS	…	Rutherford Backscattering Spectroscopy
SEM	…	Scanning Electron Microscope
Si	…	silicon

ta-C	…	tetrahedral amorphous carbon
ta-C:H	…	tetrahedral hydrogenated amorphous carbon
TEM	…	Transmission Electron Microscopy
UBMS	…	Unbalanced Magnetron Sputtering
U_m	…	potential at magnetron
U_s	…	potential at substrate holder
XPS	…	X-Ray Photoelectron Spectroscopy
XRD	…	X-Ray Diffraction
Z	…	atomic number

1 INTRODUCTION

"Thin-film technology is simultaneously one of the oldest arts and one of the newest sciences" – *Milton Ohring*

Presently, temporary metallic implants, like bone nails, based on stainless steel and titanium are widely employed. One of the major deficiencies of these implants is that they have to be removed operatively after fulfilling their task, e.g. after healing of fractured bones.

Hence, recently there are reflections about bio-degradable implants based on magnesium. They convince not only with their biocompatibility, low weight and sufficient load-bearing capacity, but also with their elastic properties closely resembling those of human bones [1]. Furthermore, magnesium is absorbed and degraded completely by the physiological environment after gradual depletion. This bio-degradation is based on corrosion of magnesium in aqueous environment, but it results in considerable gas accumulations in the surrounding tissue and injures the same [2].

The aim of this work is to provide a feasibility study on the design and development of a multifunctional coating system based on hydrogenated amorphous carbon, which is biocompatible, smooth, tough and soft. The task of this coating system is on the one hand to prevent the implant from corrosion during the healing process. On the other hand, a slow degradation of the film, which should ensure controlled access of water to the magnesium surface due to a specific porosity, should provide for a controlled degradation of the implant.

The coatings were synthesised by reactive magnetron sputtering of a graphite target in an argon/acetylene atmosphere. The basic correlations between deposition parameters, coating structure and mechanical coating properties should be accomplished.

2 Background Information

2.1 Almost everything about Carbon

2.1.1 Structure and Properties

Carbon compounds form the molecular basis of all terrestrial life, consequently carbon is very biocompatible. It is a member of the main group 4 of the periodic table, has the atomic number 6 and the symbol C. It is non-metallic and tetravalent, which means it has four electrons to form covalent chemical bonds. There are eight allotropes (Figure 2.1) of carbon, where the best known are graphite, diamond and amorphous carbon. The physical properties of carbon vary widely with the allotropic form. This shows up for example in the appearance, where graphite is opaque and diamond is transparent. While graphite is soft enough to write on a paper, diamond is known as the hardest naturally-occurring material. On the other hand, graphite is a good conductor while diamond has a low electrical conductivity.

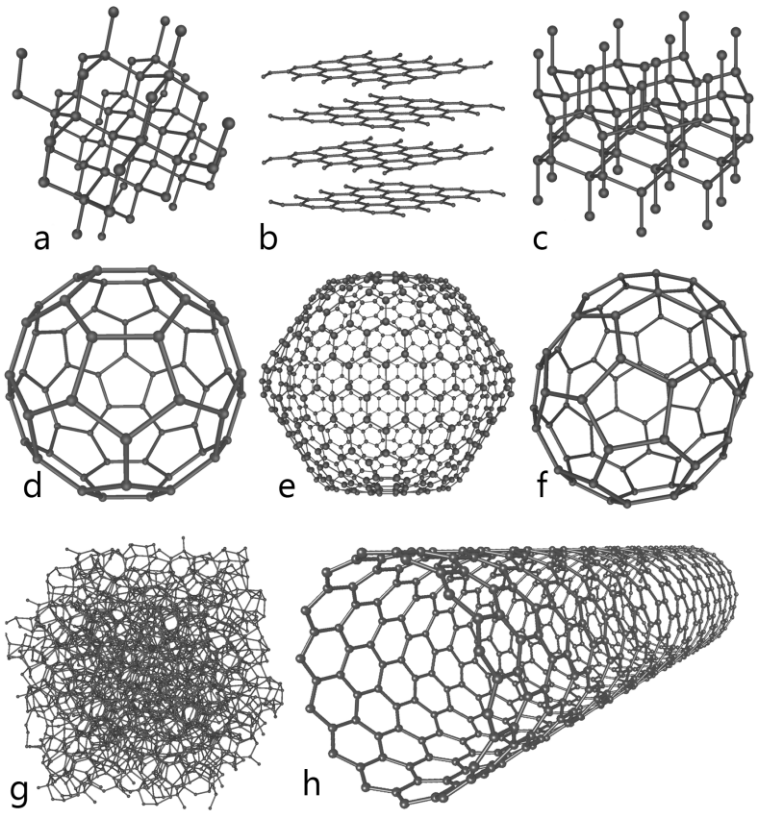

Figure 2.1: Allotropes of carbon: (a) diamond, (b) graphite, (c) ionsdaleite, (d)-(f) fullerenes (C_{60}, C_{540}, C_{70}), (g) amorphous carbon and (h) carbon nanotube [3].

Due to its special electronic configuration (L-shell half filled), carbon possesses the ability to form complex molecules and shows the greatest variety of chemical compounds. The enormous versatility of the carbon material system is based on the different bond hybridisations, i.e. sp^3, sp^2 and sp^1, as shown in Figure 2.2.

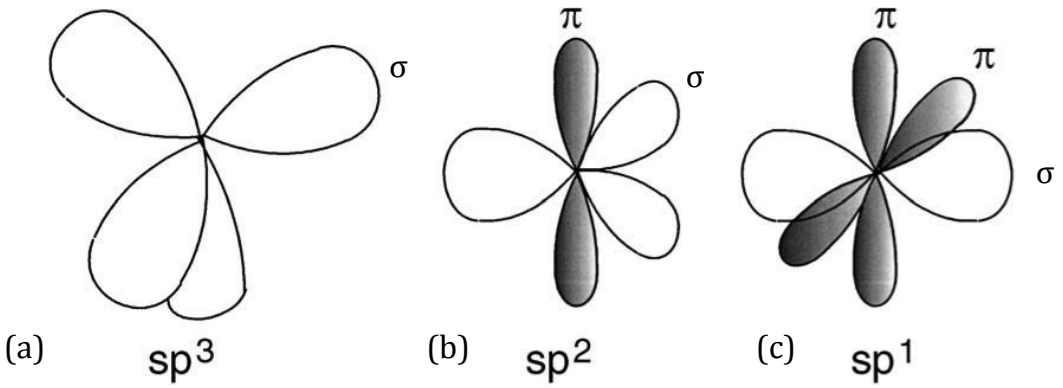

Figure 2.2: The three bond hybridisations found in carbon: sp^3, sp^2 and sp^1 [4].

The metastable sp^3 configuration, as in diamond, is a fully tetrahedral C-C bonding formation (Figure 2.2 (a)). Diamonds are not only a girl's best friend but have a very powerful image in the public and scientific community. It has the largest bulk modulus of any solid, the highest atom density, the largest room temperature thermal conductivity (900-2300 W m^{-1} K^{-1}), the smallest thermal expansion coefficient (0.8 µm m^{-1} K^{-1}), and an optical gap of 5.5 eV due to four strong σ bonds (covalent bonds) at 109.5° to each other [5].

Graphite is characterised by a fully trigonal sp^2 network that forms planar six-fold rings of single and double bonds, with weak van der Waals π bonds between the planes of its hexagonal structure. Concerning the highly delocalised π electrons along the 'c' axis (Figure 2.2 (b)), graphite has a band gap of zero [5].

The sp^1 bond consists of two strong σ orbitals along the x-axis and two further pπ orbitals in the y and z directions (Figure 2.2 (c)).

Diamond-like carbon (DLC) in general is a mixture of sp^3, sp^2 and sp^1 sites. DLC is an amorphous carbon (a-C) or hydrogenated amorphous carbon (a-C:H) thin film material with a high fraction (20-60%) of metastable sp^3 carbon bonding [6]. It is generally prepared by a deposition process involving energetic ions. The metastable sp^3 bonds transform to sp^2 under thermal or mechanical loads. DLC can have

different properties like high mechanical hardness, chemical inertness, optical transparency and a relatively wide band gap.

DLC is much less “famous” compared to diamond, but not less important than diamonds in economic terms. These coatings are used on very different applications like razor blades, in magnetic hard-disk drives, on bar-code scanners, on PET bottles, on some car parts and on medical devices.

2.1.2 Phase Diagram

The different carbon phases can be displayed in a ternary phase diagram shown in Figure 2.3. The phase diagram was first established by Jacob and Moller [7] and illustrates the fraction of sites in the C-matrix that are C sp^3, C sp^2 or hydrogen (H).

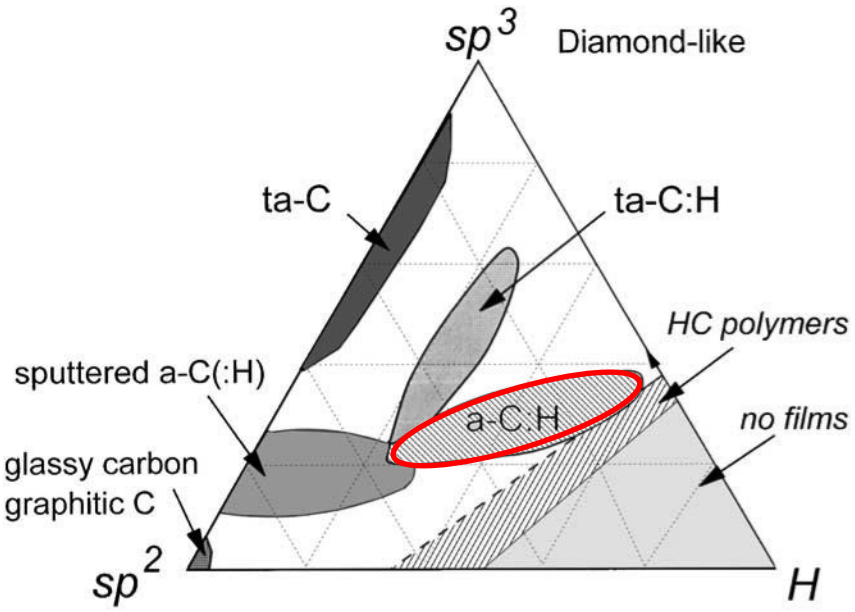

Figure 2.3: Ternary phase diagram of the C-H system [7].

Three main sections in this ternary phase diagram can be distinguished. Along the sp^2-sp^3 axis there is the H-free a-C region. The sp^2 a-C is characteristically glassy carbon and not DLC and is made by evaporation or by pyrolysis of hydrocarbon polymers.

Sputtered DLCs with quite large sp^3 content, still without H, can be prepared for example with unbalanced magnetron sputtering [8]. If the sp^3 content further increases, there is a specific type of a-C called tetrahedral amorphous carbon (ta-C). Due to its high sp^3 content, the properties are more like diamond than graphite.

In the hydrogen rich corner the compounds have gaseous nature [7].

The boundary line of this second region is defined by the compositions of acetylene (C_2H_2) on the sp^2-H axis and methylene ($(CH_2)_n$) on the sp^3-H axis. The a-C:H materials are situated within these regions. They can be produced by reactive sputtering of graphite in a hydrogen-containing atmosphere, by plasma-enhanced chemical vapour deposition (PECVD) of hydrocarbon molecules, or by ion beam deposition from a hydrocarbon gas precursor. These a-C:H films can have H contents from 20 up to 60% [8] and compared with ta-C they are polymeric, softer and tougher.

With so-called high-density plasmas, denser a-C:H films can be produced called tetrahedral hydrogenated amorphous carbon (ta-C:H).

DLC has some extreme properties similar to diamond, like hardness, elastic modulus and chemical inertness. Apart from that, it forms isotropic disordered thin films without grain boundaries [6].

2.2 Deposition Technique – Sputtering

2.2.1 Fundamentals of Sputtering

Sputtering is a vacuum process where incident inert gas ions, usually Ar^+ ions, eject atoms or clusters from a solid target material which transfer into a gaseous phase due to momentum transfer. These positive ions are generated in a glow-discharge ignited between two electrodes, where the target is the cathode and the substrate holder or the chamber wall forms the anode (Figure 2.4 (a)).

The incident gas ion transfers its impulse to the target atoms, which trigger further collisions like a shock cascade. After several collisions some of the momentum point towards the surface. Atoms knocked on by this momentum may leave the target if they have enough energy and if they are near the surface (Figure 2.4 (b)). The ejected atoms condense on the substrate that is positioned near the target (Figure 2.4 (c)).

Sputtering is done in vacuum in the pressure range of 10^{-3} - 10^{-2} mbar to reduce the collision probability of sputtered species with gas atoms.

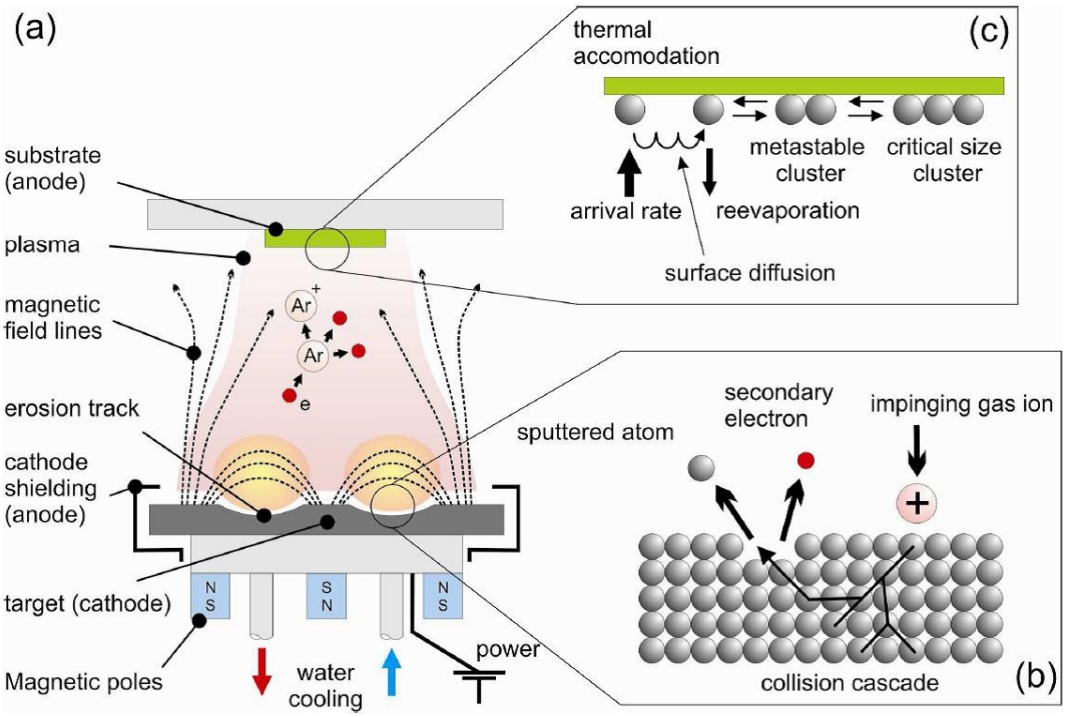

Figure 2.4: (a) Schematic illustration of a magnetron sputtering system showing the most relevant processes during (b) a sputter procedure at the target and (c) the nucleation process at the sample surface [9].

Generally a direct current (DC) gas discharge serves as an ion source. The target acts as negative (cathode) and the substrate as positive electrode (anode). If there is a permanent magnetic field beneath the target, the so-called magnetron sputtering can be put into practice. It can be categorised into two types:

- conventional balanced magnetron sputtering (CBMS) and
- unbalanced magnetron sputtering (UBMS).

In CBMS, all magnetic field lines are closed between the poles. In UBMS, the field lines are partially open towards the substrate. It is realised by using stronger outer or inner magnets. Figure 2.5 illustrates schematic diagrams of CBMS and UBMS processes.

Due to the interaction between the electric and magnetic field, the charge carriers move in spirals instead of parallel so that they circulate above the target surface. As a result their way extends and the number of collisions per electron rises.

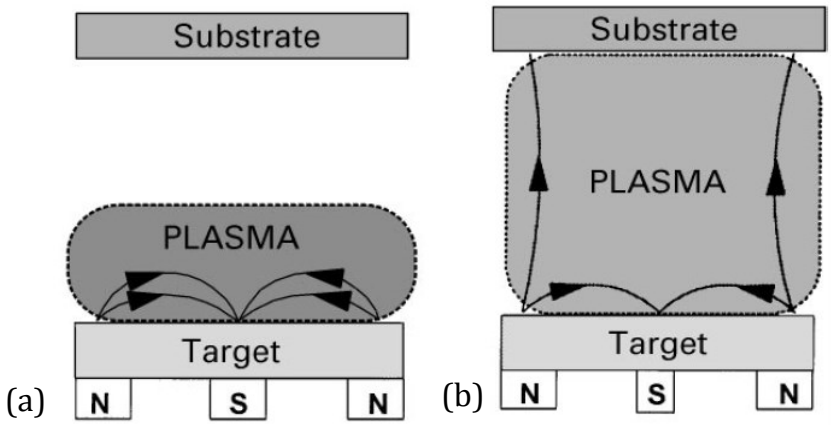

Figure 2.5: Schematic illustration of (a) a balanced and (b) an unbalanced magnetron [10].

2.2.2 Reactive Sputtering

In general, to produce alloys or compounds reactive sputtering is a common technique besides sputtering with multicomponent or different single element targets. There, at least one component of the film originates from the gas phase. Additionally to the inert working gas, for example argon, a particular fraction of reactive gas, for example acetylene (C_2H_2) or nitrogen (N_2), is introduced into the vacuum chamber.

Three different reactions are possible to form the compound [11] [12]:

- The compound is formed at the target surface and these molecules are sputtered.
- The compound is formed in the gas phase.
- The reactive gas is adsorbed on the substrate and subsequently there is a reaction with the impinging target atoms.

Whereas the compounds formed at the target surface are estimated to be sputtered as single atoms and due to the low probability of collisions between sputtered atoms, reactive gas molecules and ions/electrons in the gas phase, the third reaction is the most important one. An advantage of reactive sputtering is that with modifying the partial pressure of the reactive gas, the stoichiometry of the resulting film can be adjusted. By employing simple metallic targets and providing several components in the gas phase, even very complex films can be produced [13].

2.3 Raman Spectroscopy

The Raman effect was first described by Chandrasekhara Venkata Raman [14]. It is based on inelastic scattering of monochromatic light, usually from a laser in the visible, near infrared or near ultraviolet range, with phonons or other excitations in the atomic system (Figure 2.6) to estimate for example phase composition, crystallinity or stresses.

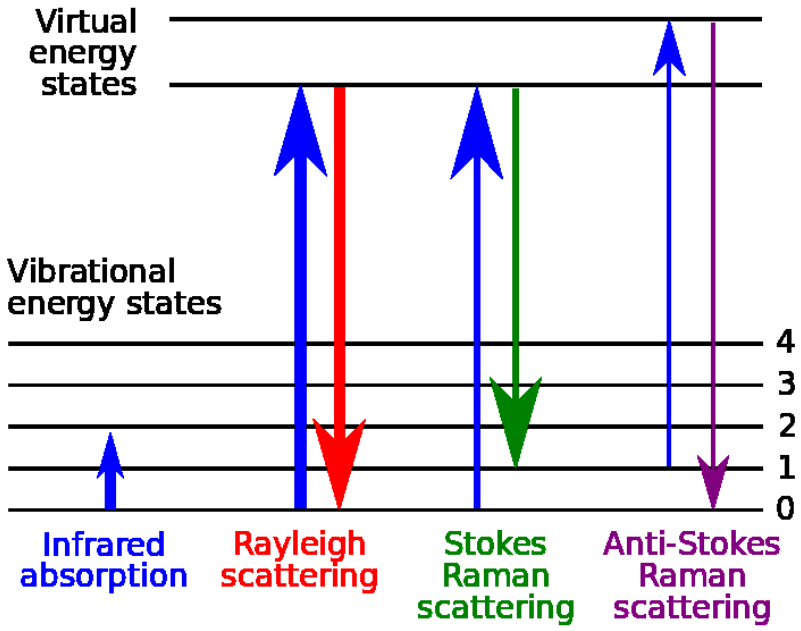

Figure 2.6: Photon-phonon interaction in Raman spectroscopy [15].

The energy of the laser photons is shifted up or down and this shift gives information about the phonon modes in the system. Raman spectroscopy is known to be the most convenient method of bonding structure investigations of carbon materials. Each configuration of carbon has its own typical Raman spectra, as shown in Figure 2.7. Diamond and single crystalline graphite have single Raman active modes at 1332 cm^{-1} and 1580 cm^{-1}, respectively. In single crystalline graphite, the mode is labelled 'G' for 'graphite'. The G-mode is the stretching vibration of any pair of sp^2 sites, no matter if in chains or aromatic rings [16]. Disordered graphite, like DLC, has a second mode at about 1350 cm^{-1} labelled 'D' for 'disordered', which is the breathing mode of the sp^2 sites just in rings, not in chains (Figure 2.8). In single crystalline graphite this mode is forbidden [16].

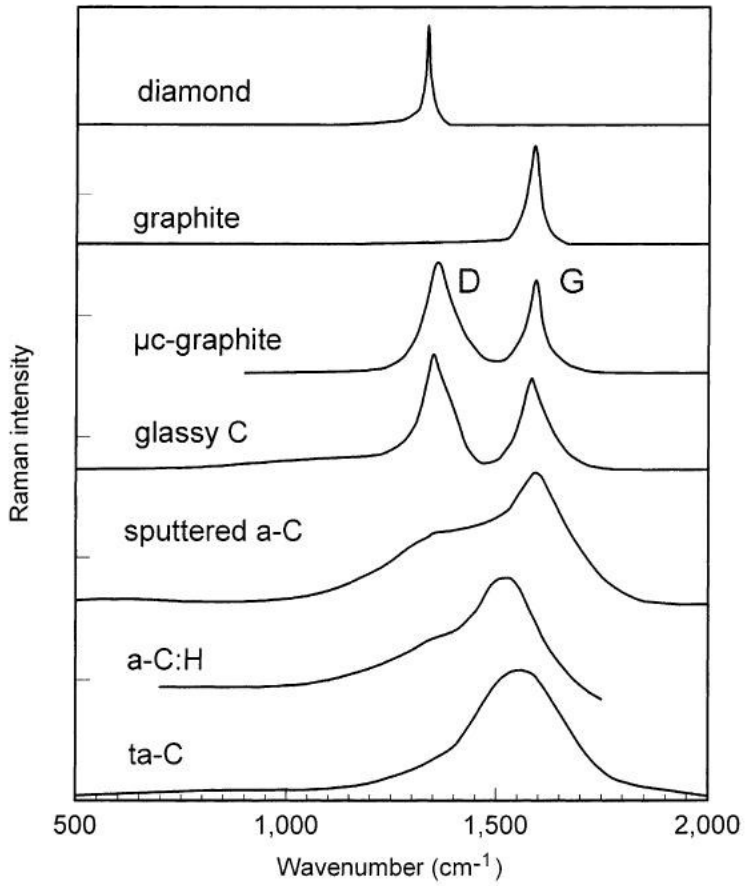

Figure 2.7: Comparison of different carbon Raman spectra [6].

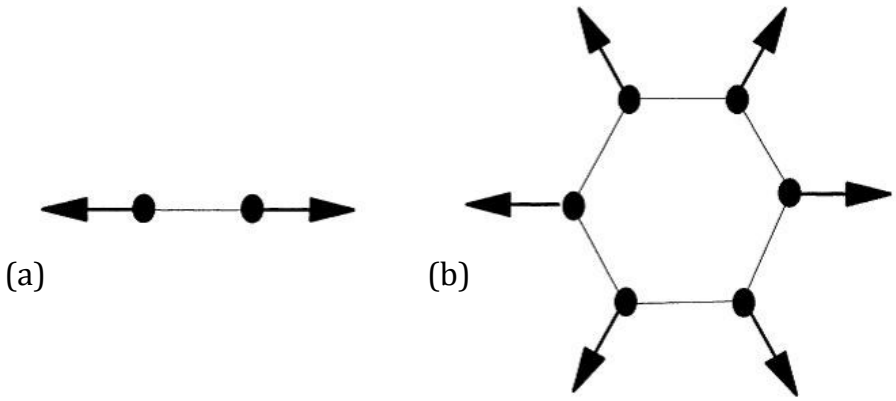

Figure 2.8: (a) G mode in graphite and (b) D mode in amorphous carbon [16].

These G and D modes dominate the Raman spectra of each disordered graphite film. Various factors as shown in Figure 2.9 can shift the peaks in either direction and vary their relative intensity.

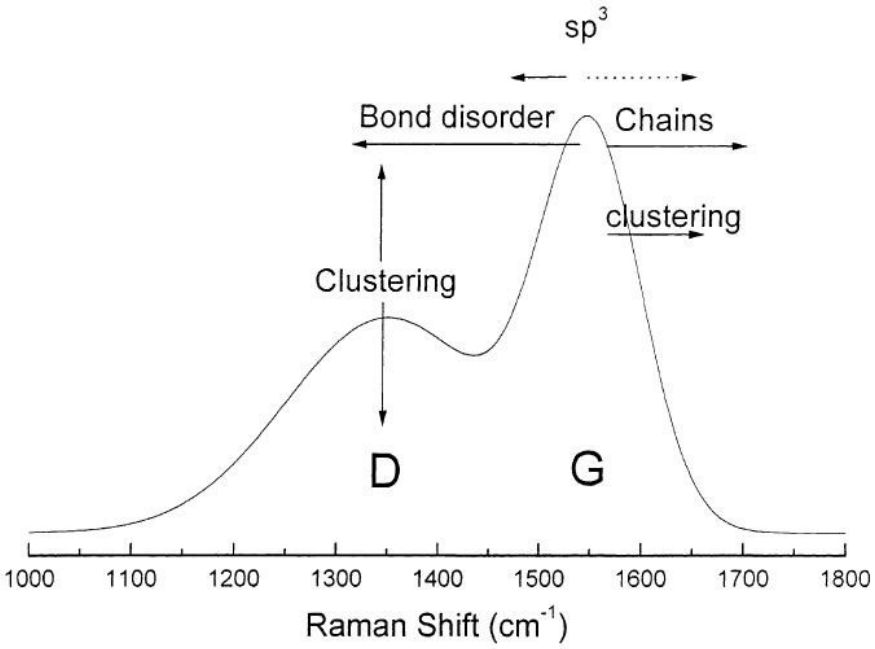

Figure 2.9: Schematic Raman spectrum of amorphous carbon showing the factors affecting the position and height of G and D peak [16].

Before analysing the Raman spectra it is important to know which method has been used to fit the spectra because this influences the numerical values. In this work, the spectra were fitted with a Gaussian distribution function (Figure 2.10). In a Gaussian fit, the areas of the fitted D- and G-band are used for estimating the intensity ratio I_D/I_G.

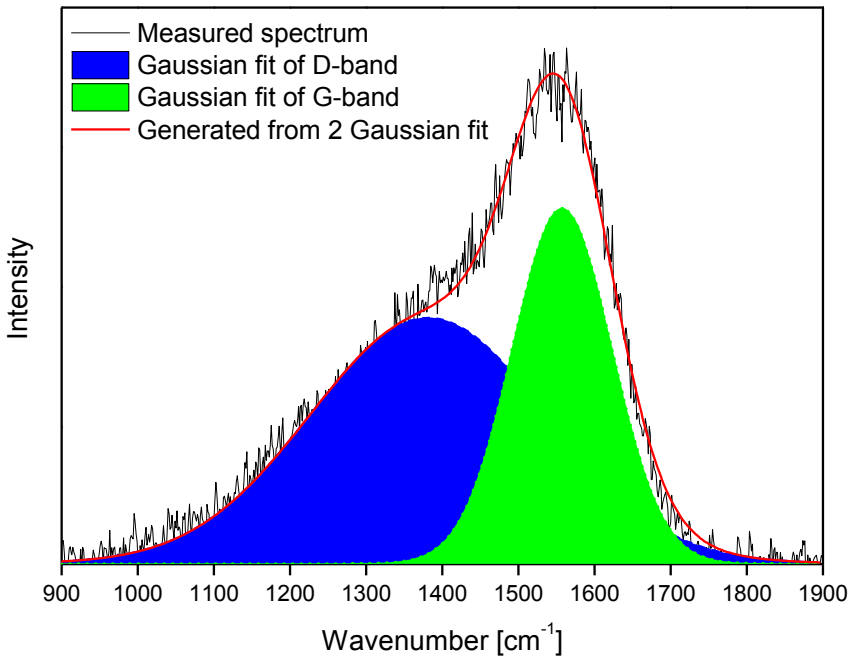

Figure 2.10: Gaussian fit of D- and G- band [own work].

The Raman spectrum of a-C is sp^2 site dominated and according to this there is no direct information about the sp^3 bonding fraction via visible light excitation.

Investigations of the I_D/I_G ratio of the considered disorder structure show an indirect correlation. Due to the fact that the sp^2 site disorder is influenced by the sp^3 fraction, the I_D/I_G ratio can be inversely used to get information about the sp^3 fraction existing in the a-C phase [6] [17]. Hence, the sp^2 fraction can be gauged by the hybridisation ratio:

$$\frac{I_D}{I_G} \sim sp^2 \sim \frac{1}{sp^3} \tag{1}$$

Ferrari and Robertson [16] suggested classifying all Raman spectra of disordered carbon within a three-stage model of increasing disorder. In Figure 2.11 these three stages are shown.

1. perfect graphite to nano-crystalline graphite
2. nano-crystalline graphite to a-C
3. a-C to ta-C

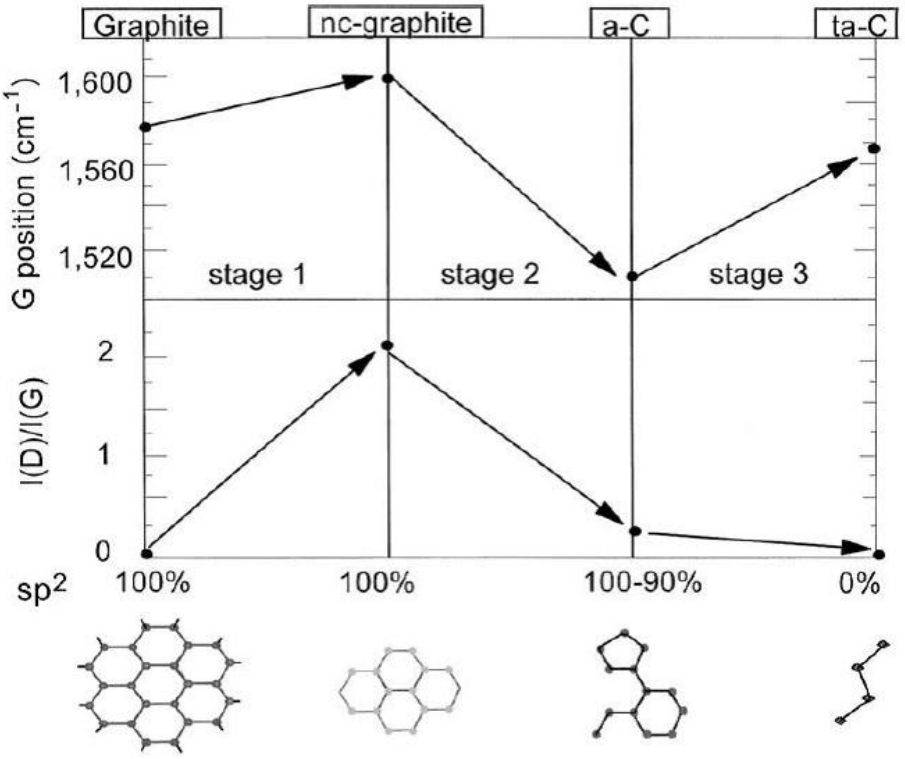

Figure 2.11: Schematic trajectory of the Raman G peak wavenumber and I_D/I_G ratio with degree of disorder [adapted from [16]].

Stage 1 is in accordance with the structural change from perfect graphite to nano-crystalline graphite with the following main changes in the Raman spectra [16]:

- The G-band moves from 1580 to ~1600 cm-1.
- The D-band appears and the intensity ratio ID/IG increases.

Reference [16] explains these variations in detail.

Stage 2 corresponds to the structural change from nano-crystalline graphite to a-C and at the end of this stage, there is a completely disordered, almost fully sp^2 bonded a-C network consisting of distorted six-fold rings or rings of other orders [16]. The main changes in the Raman spectra are [16]:

- The G-band moves from ~1600 to 1510 cm-1.
- The intensity ratio ID/IG decreases, which means a decrease of the number of ordered sp^2 rings.

Stage 3 is equivalent to the structural change from a-C to ta-C, which means the sp^3 content increases from ~10 to ~85% [16] and the sp^2 sites change successively from rings to chains. The main changes in the Raman spectra are [16]:

- The G-band moves from ~1510 to 1570cm-1.
- The intensity ratio ID/IG decreases nearly to zero.

This structural evolution through these three stages is called amorphisation trajectory or disordering trajectory, whereas in the reverse direction it is called ordering trajectory.

3 Experimental Methods

3.1 Sputter Deposition

3.1.1 Deposition System

All coatings for this work were deposited using a modified Leybold-Heraeus Z 400 DC reactive unbalanced magnetron sputtering device, as schematically shown in Figure 3.1 [18] [19].

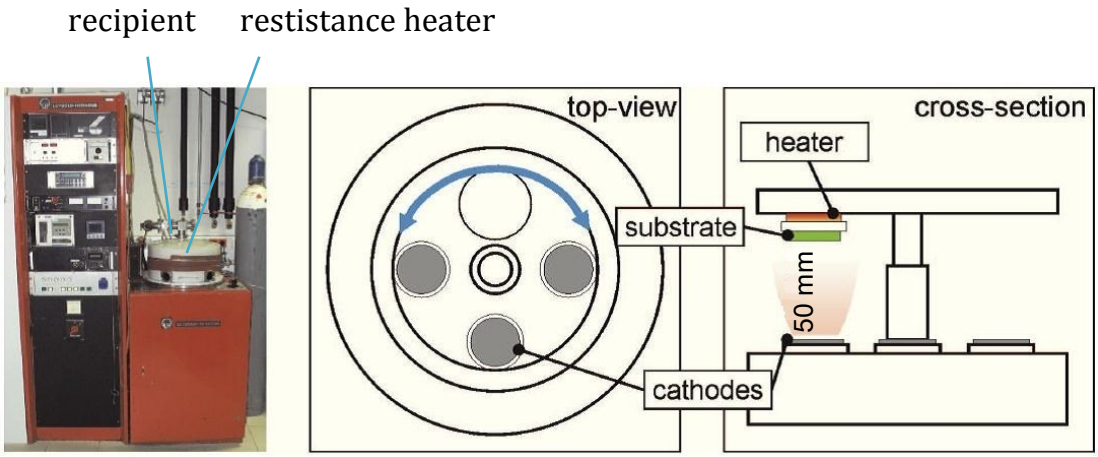

Figure 3.1: Schematic construction of the deposition chamber [9].

The sputtering system consists of a cylindrical recipient (∅ 420 mm × 200 mm), which contains space for three water cooled magnetrons. The magnetrons are horizontally fixed and for this thesis just one carbon target (∅ 75 mm × 6 mm) was situated on one magnetron and the other two were covered.

The substrate holder is mounted on a horizontal rotary device at a distance of ~50 mm from the target. For the sputtering process it is positioned above the magnetron.

The discharge is ignited between the magnetron and the substrate holder. An MKS ENI RPG-50 pulsed DC power supply (frequency 250 kHz, duty cycle of 496 ns – 40%) was applied for plasma etching of the substrates by using a negative bias voltage of -500 V. After etching the bias voltage was reduced to -50 V during deposition. A modified Leybold-Heraeus power supply was used to provide the magnetron with a maximum power of 2 kW. For the required vacuum inside the deposition chamber, a dual stage rotary vane pump (Pfeiffer DUO 20, [20]) and a

turbomolecular pump (Leybold Turbovac 361, [21]) were utilised. Furthermore, outside the recipient a resistance heater was attached to bake out the chamber. A residual pressure of less than 2×10^{-5} mbar was reached.

3.1.2 Calibration of the Sputter System

In order to estimate the gas pressure for deposition, two calibration runs were done. The first one, shown in Figure 3.2, was done for the working gas (argon) for a flow rate from zero to 40 sccm. For argon a correction factor of 0.83 has to be considered [19], which shows up in the corrected chamber pressure.

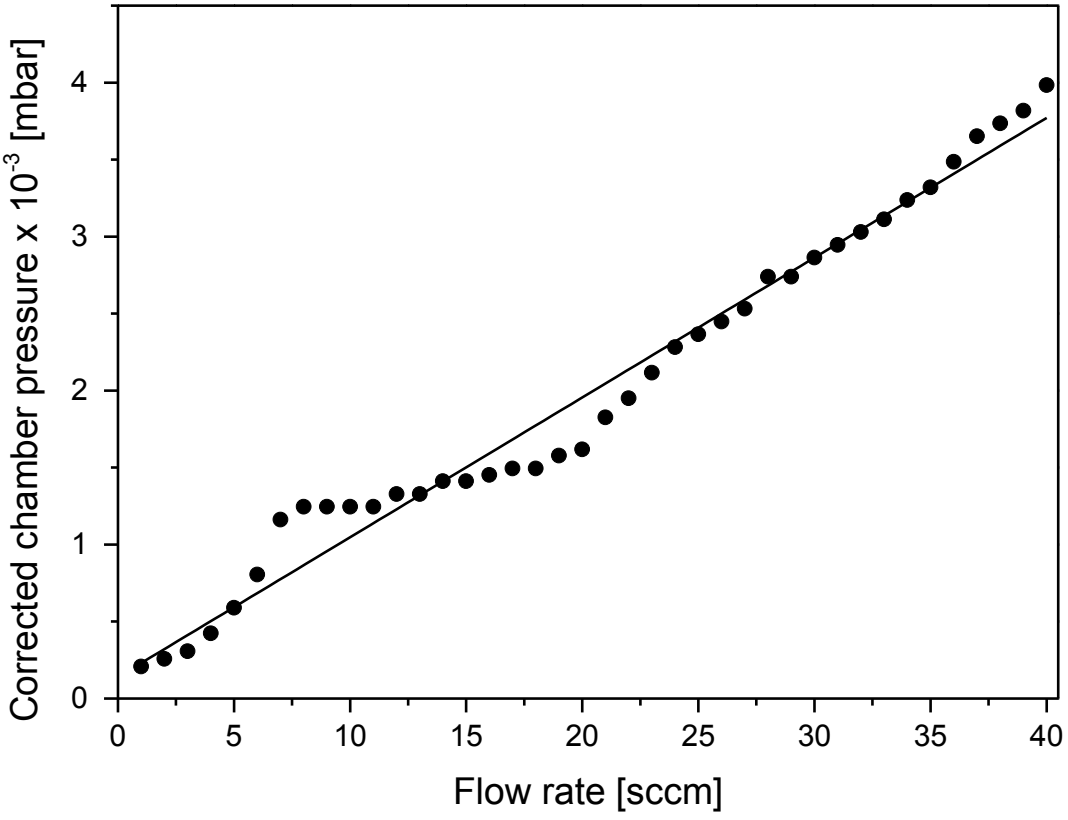

Figure 3.2: Corrected flow rate of the working gas (argon).

The second calibration run, shown in Figure 3.3, was done for the reactive gas (C_2H_2) for a flow rate from zero to 20 sccm. For this hydrocarbon, the correction factor is between 0.1 and 0.4 [19].

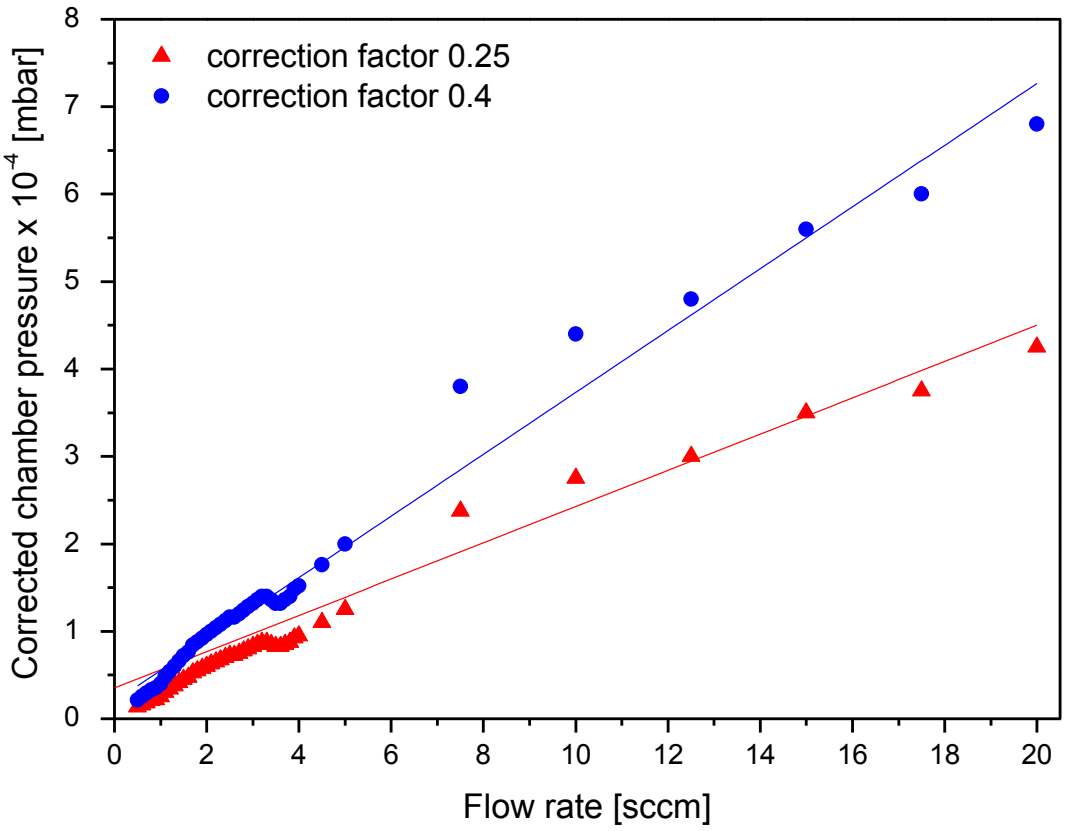

Figure 3.3: Corrected flow rate of the reactive gas (C_2H_2) calibrated with two different correction factors.

These calibration curves are important for the deposition process, because every gas has its own partial pressure and contributes to the total pressure with different amount due to the prevalent gas mixture.

3.1.3 Sputter Procedure

All variants of the coating were deposited on Si (100) (20 mm × 7 mm × 0.380 mm) wafers. Prior to deposition, the substrates were ultrasonically cleaned in acetone and ethanol for 5 min each and dried by a hot air gun.

For further substrate cleaning, they were plasma etched for 15 min after evacuating the chamber to a total pressure of less than 1×10^{-5} mbar. For plasma etching, the Ar (99.999% purity) gas flow was set to 40 sccm, which lead to a total pressure increase up to 10^{-2} mbar. A negative bias voltage of –500 V was applied to force collisions of the Ar^+ ions with the substrate surface. After etching, the Ar gas flow was turned off and the chamber was evacuated to a total pressure below 4×10^{-6} mbar again.

All deposition runs were carried out for 30 minutes. No external heating of the substrate holder was used resulting in an estimated temperature of 200°C. The gas flow of Ar (working gas) was kept constant at 10 sccm for all depositions and the C_2H_2 (reactive gas) gas flow gradually increased from 0 to 10 sccm, resulting in a partial pressure variation as shown in Figure 3.2 and Figure 3.3. After deposition the chamber was cooled down for one hour with a resulting total pressure of about 4×10^{-6} mbar. Table 3.1 shows the deposition parameters of all runs.

Table 3.1: Deposition parameters

Sample name	**flow (Ar)**	**flow (C_2H_2)**	**total pressure**	**BIAS U_s**	**BIAS I_s**	**P_m**	**U_m**	**I_m**
	[sccm]	**[sccm]**	**[mbar]**	**[V]**	**[mA]**	**[W]**	**[V]**	**[mA]**
aCH-0	10	0	8.1×10^{-3}	-50	80	400	595	610
aCH-2	10	2	1.1×10^{-2}	-50	80	400	553	670
aCH-4	10	4	1.4×10^{-2}	-50	80	400	532	700
aCH-6	10	6	1.7×10^{-2}	-50	80	400	517	730
aCH-8	10	8	2.0×10^{-2}	-50	80	400	539	690
aCH-10	10	10	2.2×10^{-2}	-50	80	400	616	670

3.2 Coating Characterisation

3.2.1 Coating Thickness

The coating thickness *d* was measured at the Materials Center Leoben with a scanning electron microscope (SEM, Zeiss SMT Auriga) by cutting into the sample (Figure 3.4) with a focused ion beam (FIB, Orsay Physiks Cobra Z-05).

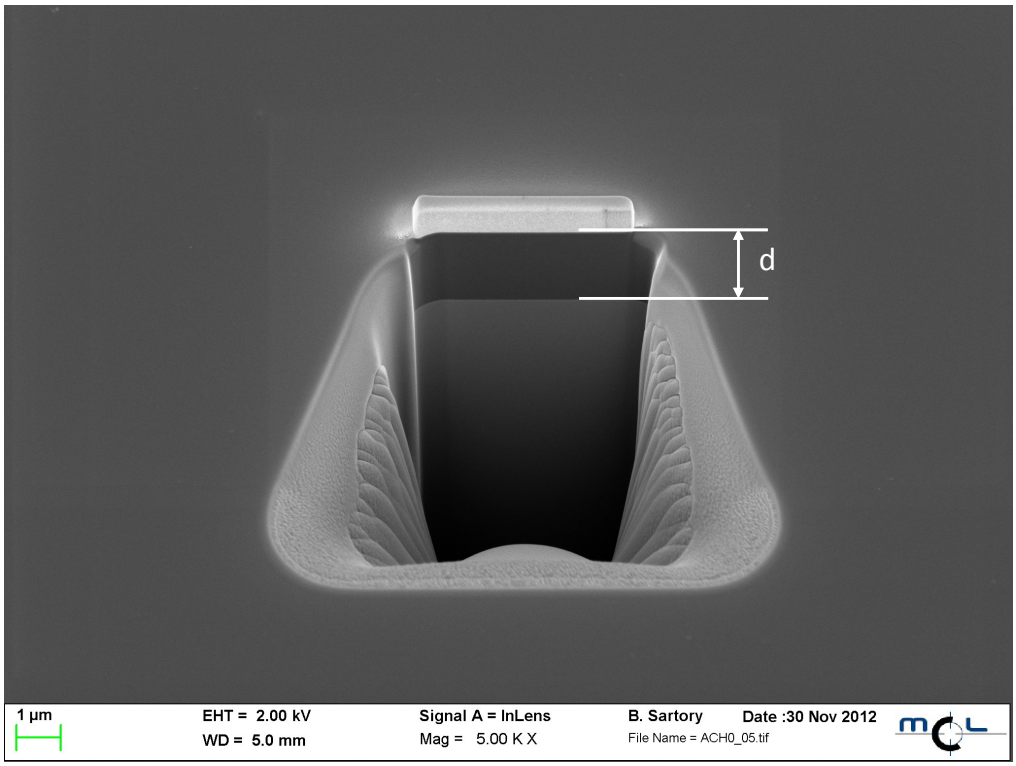

Figure 3.4: FIB cut for coating thickness measurement.

3.2.2 Elastic Recoil Detection Analysis (ERDA)

ERDA is deemed to be the most convenient method to determine the hydrogen content in DLC films. L'Ecuyer et al. first established the formalism for this determination in 1976 [22]. It is based on the detection of light nucleus recoil from a target bombarded by energetic ions [23]. The energy of a recoil nucleus E_1 is defined through the following equation [23]:

$$E_1 = E_0 \frac{4M_1M_2}{(M_1 + M_2)^2} \cos^2 \theta \qquad (2)$$

There, E_0 is the projectile particle initial energy, M_1 and M_2 are the masses of the projectile and the target atom and θ is the recoil angle. In Figure 3.5 the collision between an incident ion M_1 and a target atom M_2 is schematically shown.

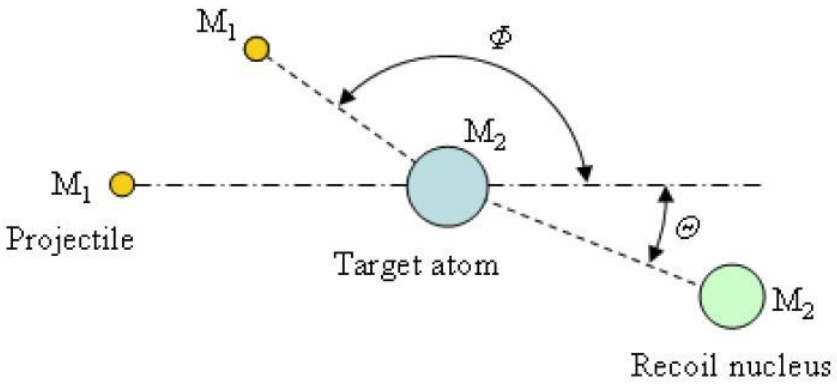

Figure 3.5: Schematic collision process [adapted from [23]].

The relation between the scattering angle ϕ (RBS) and the recoil angle θ (ERDA) characterises the geometry of the collision [23]:

$$\cos^2\theta = \frac{(M_1M_2)^2 - (M_1\cos\phi \pm \sqrt{M_2^2 - M_1^2\sin^2\phi}))^2}{4M_1M_2} \quad (3)$$

In this work, ERDA measurements were carried out at the Helmholtz-Centre Dresden-Rossendorf using a 35 MeV Cl^{7+} ion beam. The angle between the sample normal and the incoming beam was set to 75°, the scattering angle was set to 31°. The analysed area was about 1.5 × 1.5 mm^2. The recoil ions have been detected with a Bragg ionisation chamber using a full energy detection circuit for the ion energies and a fast timing circuit to obtain a Z (atomic number) dependent signal to separate ion species. H has been detected with a separate solid state detector at a scattering angle of 41° preceded by an 18 µm Al foil to stop other scattered and recoiled ions.

3.2.3 X-Ray Diffraction (XRD)

The measurements were carried out with a Bruker-AXS D8 Advance diffractometer using Cu Kα radiation. The detector scan mode with a grazing incidence angle of 2° and a 2θ angle between 10 and 100° was used. The operating parameters shown in Table 3.2 were kept constant for all measurements.

Table 3.2: Operating parameters of the Bruker-AXS D8 Advance diffractometer.

High Voltage [kV]	Tube Current [mA]	Step Time [s]	Step Size 2θ [°]
40	40	1.2	0.02

3.2.4 X-Ray Photoelectron Spectroscopy (XPS)

With XPS the elemental composition as well as the chemical and electronic state of elements within a material can be determined. The material is irradiated with a X-ray beam while simultaneously the kinetic energy and number of electrons escaping is measured. In this work, XPS was used to determine the contribution of the binding energy E_B of the C1s orbital of carbon, which gives information about the sp^2 and sp^3 content:

$$E_B = E_{Ph} - (E_K + \phi) \tag{4}$$

There, E_B is the binding energy of the electron, E_{Ph} is the known energy of the X-ray photons (composed of $h\nu$; with h as Planck's constant and ν as radiation frequency), E_K is the kinetic energy of the electron as measured by the instrument and ϕ is the work function of the spectrometer.

Within this work, the measurements were carried out at the Chair of Chemistry of Polymeric Materials at the Montanuniversität Leoben with a Thermo Scientific K-Alpha X-ray Photoelectron Spectrometer. The parameters are listed in Table 3.3.

Table 3.3: Used acquisition parameters for XPS.

No. Scans	Source Type	Spot Size [µm]	Lens Mode	Analyser Mode	Energy Step Size [eV]
3	Al Kα	400	Standard	CAE : Pass Energy 50.0 eV	0.1

3.2.5 Raman Spectroscopy

In this work Raman spectroscopy was used to determine the ratio of I_D/I_G, which means to estimate the ratio of sp^2/sp^3 content of the films. The measurements were carried out by using a Horiba Dilor Raman spectroscope with a laser wavelength of 532.2 nm (Nd:YAG laser) at a power level of 100 mW (3.5 mW at the measurement point). Different filters were used to reduce the intensity of the laser to avoid damaging of the film. The recorded data were fitted with the Gaussian method and compared with literature.

3.2.6 Nanoindentation

The hardness and Young's modulus were quantified with a Nanoindentor System (UMIS, Fischer-Cripps Laboratories). All measurements were carried out with a Berkovich diamond tip with a tip radius less than 200 nm. In literature the indentation depth is commonly controlled to the ≤ 1/10 rule of thumb for hardness measurements [24]. A test series with decreasing load starting at 10 mN and a step size of 1 mN was done.

Two essential conditions have to be considered for meaningful measurements:

- no appreciable substrate influence
- a fully-developed plastic zone below the indent.

The hardness was calculated on the basis of the load-displacement curve (Figure 3.6):

$$H = \frac{P}{A} * \frac{A_i}{A} \tag{5}$$

There, P is the indentation load, A is the contact area and $\frac{A_i}{A}$ is the area function, which is used to correct a not exactly sharp tip.

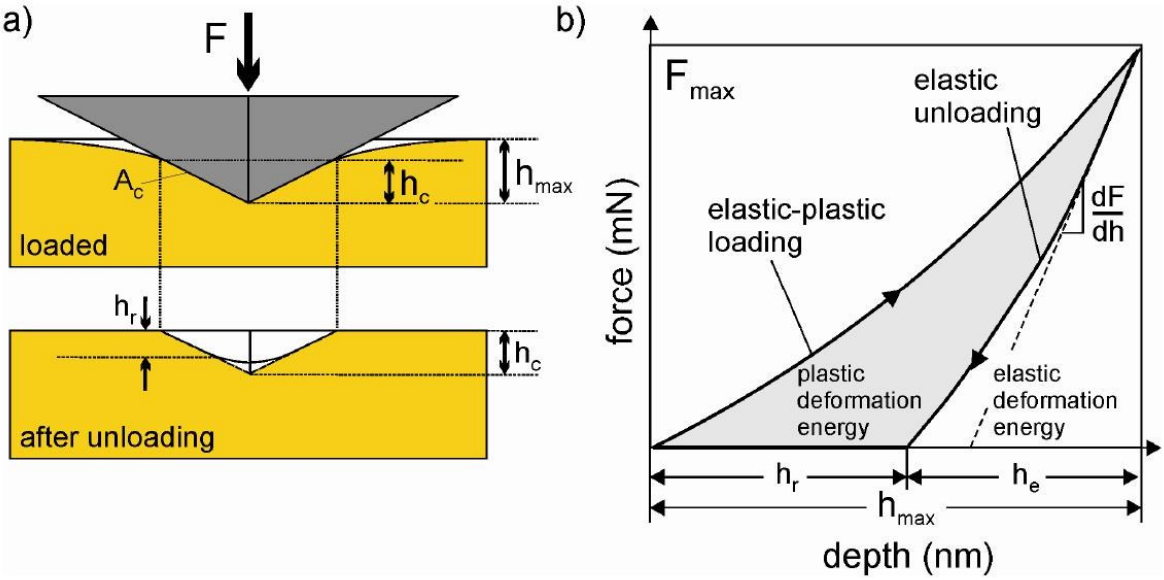

Figure 3.6: a) Schematic illustration of an indentation and b) a typical load-displacement curve showing elastic and plastic contributions [25].

The Young's modulus was calculated by the method of Oliver and Pharr [26]:

$$E^* = \frac{dP}{dh}\frac{\sqrt{\pi}}{2\beta\sqrt{A}}\sqrt{\frac{A_i}{A}} \tag{6}$$

There, dh is the indentation depth, $\frac{dP}{dh}$ is the stiffness of the material and β is the indenter geometry factor.

3.2.7 Residual Stresses

After deposition, there are intrinsic and thermal stresses in the film. Consequently, the coated substrate bends (Figure 3.7 (a)) and can cause failure like delamination of the film. Stresses can be determined by measuring the curvature of the surface.

In this thesis, a laser based optical testing method was used to determine the stress levels at room temperature and enhanced temperatures [27].

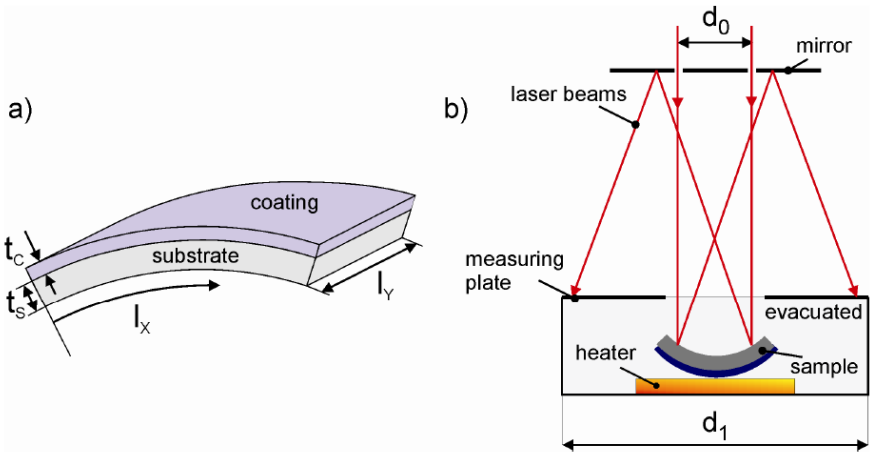

Figure 3.7: a) Schematic illustration of a curved substrate/coating composite due to residual stresses and b) laser based biaxial stress measurement with parallel laser beams [adapted from [27]].

The samples were positioned in a vacuum chamber to ensure stable measurement conditions. Subsequently, the chamber was evacuated to a total pressure of 5×10^{-5} mbar. The measurement started at room temperature and went up to 700°C in steps of 50°C. To measure the curvature of the surface due to internal stress, two parallel He-Ne-laser beams (λ=632.8 nm, beam diameter: 1.2 mm) were used, which were first reflected from the sample surface and then from a mirror (Figure 3.7 (b)). These beams were projected to a white surface where they are detectable as two points. The distance of these points was measured both during heating and cooling and is proportional to the radius of curvature of the sample. The radius of curvature R of the coated silicon substrates was calculated with:

$$R = \frac{2hd_0}{d_1 - d_0} \tag{7}$$

There, h is the distance between film surface and mirror, d_0 is the initial distance between the two laser beams and d_1 is the measured distance after reflection, see Figure 3.7. For the calculation of the nominal stress σ_f, the modified Stoney formula was used:

$$\sigma_f = M \frac{t_s^2}{6t_c} \frac{1}{R} \tag{8}$$

There, M is the biaxial modulus of the substrate, t_s is the thickness of the substrate, t_c is the thickness of the coating and R is the radius of curvature of the substrate [27].

4 RESULTS

4.1 Coating Thickness

Figure 4.1 illustrates a representative FIB cut, showing substrate (grey) and coating (dark grey), where the coating thickness *d* was measured. The micrograph indicates good adhesion between substrate and coating without any cracks. The film appears dense without pores or holes, it shows an amorphous structure with uniform thickness and smooth surface (see also the lower magnification micrograph in Figure 3.4).

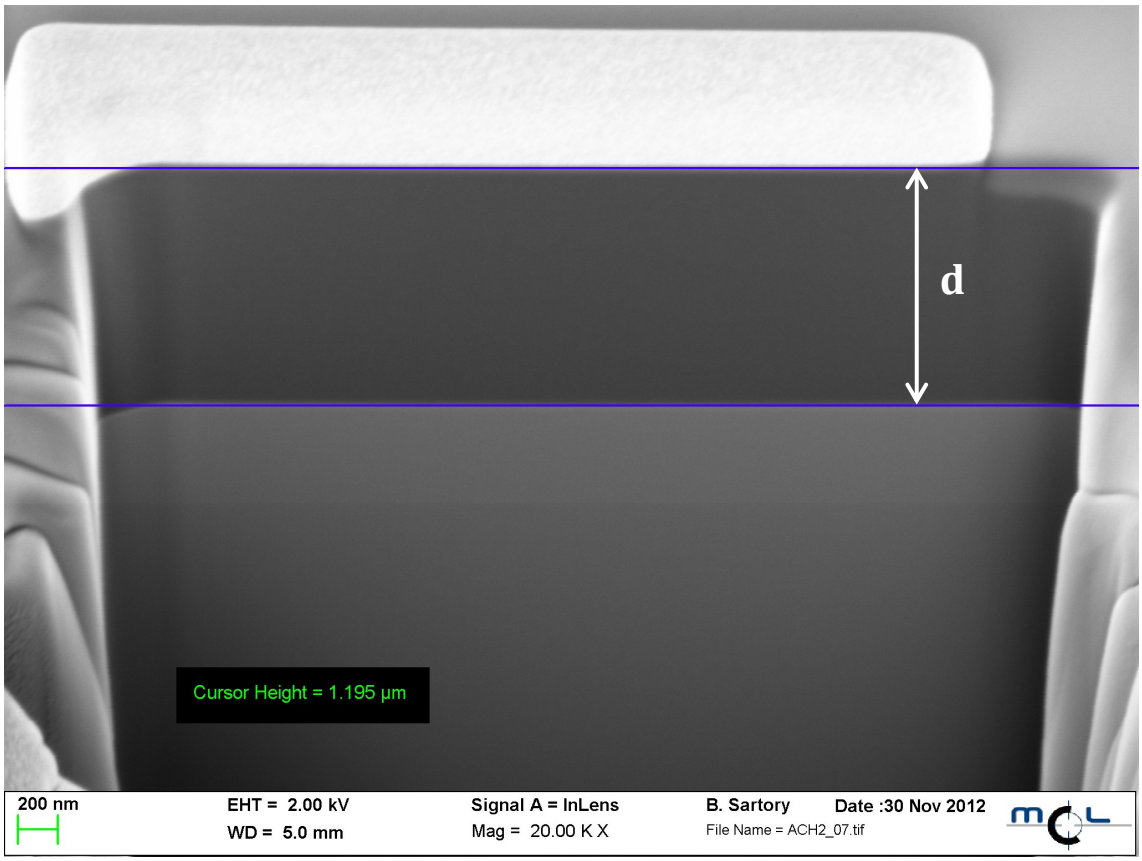

Figure 4.1: FIB cut for measuring the coating thickness (sample aCH-2).

The measured film thicknesses increase from 1.4 (without C_2H_2) to 2.2 µm (with C_2H_2/Ar flow ratio of 1.0), which results in a film growth rate from about 2.5 up to nearly 5.0 µm per hour. Figure 4.2 shows this increase of the growth rate due to an

increasing C_2H_2/Ar flow ratio. Up to a flow ratio of 0.4, the growth rate seems to be nearly constant. But above, the reactive gas contributes significantly to the film growth, resulting in considerably higher growth rates [28]. The standard deviation of 5% is due to calculated measuring inaccuracy.

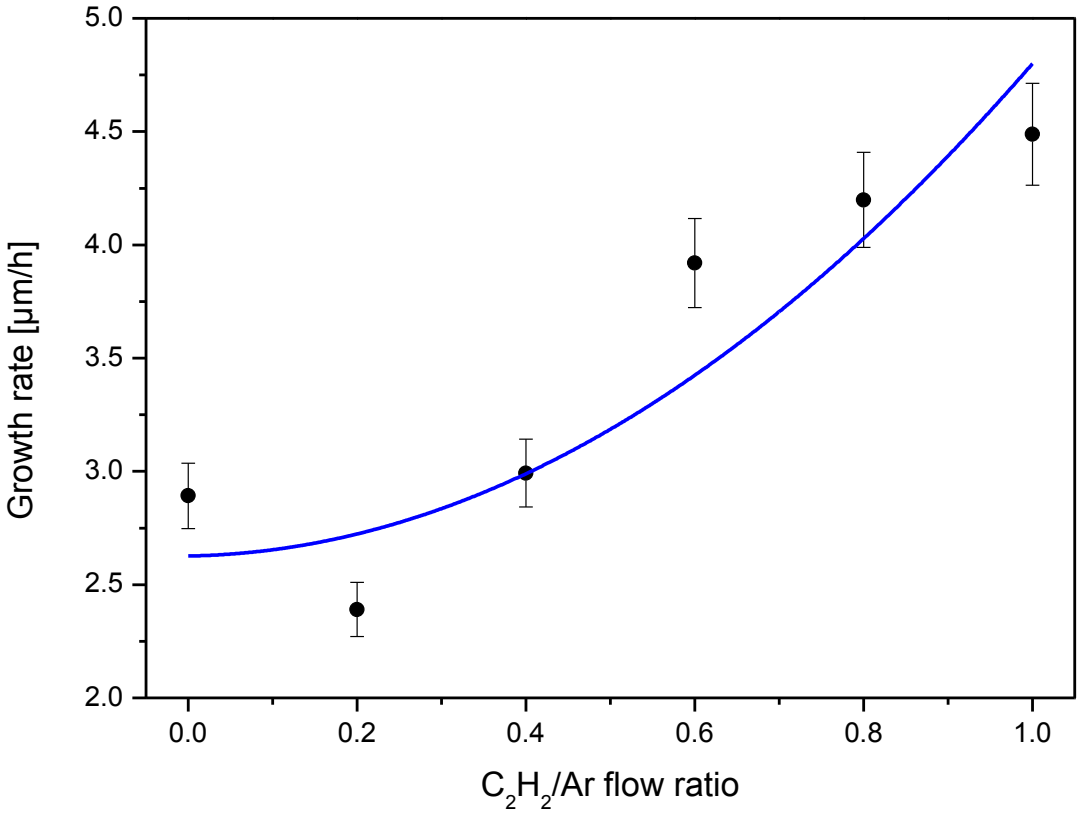

Figure 4.2: Film growth rate as a function of the C_2H_2/Ar flow ratio.

4.2 Elastic Recoil Detection Analysis

The results of the ERDA measurements for all samples are summarised in Table 4.1. All coatings have an average H-content of 20 at %. The contamination of oxygen is below 0.3 at % and for nitrogen it is between 0.3 and 0.9 at %. The relatively low content of contamination indicates a constant overall condition of the deposition system without any leaks. The coating with a flow ratio of 0.2 shows a slightly lower H-content of 16 at % and on the other hand a slightly higher contamination with nitrogen (1.5 at %). The contamination of Ar in the film is due to the bombardment with Ar^+ ions [29]. The amount of Si found for the sample with a flow ratio of 1.0 is around the detection limit. This means that the element is present but the uncertainty in the value is very large. The measured thickness of 7×10^{18} at/cm^2 corresponds to a film thickness of about 640 nm with an assumed density of 1.8 g/cm^3. For comparison, Kahn [30] found an H-content of 28 at % for a C_2H_2/Ar flow ratio of 0.43. There, the higher H-content at lower flow ratio might be due to several effects not specified in [30] like different deposition distance, varying power supplied to the target or different bias voltage at the substrate.

Table 4.1: The average chemical composition of the coatings as determined by ERDA.

Sample	Ar	Si	O	N	C	H
	[at %]	[at %]	[at %]	[at %]	[at %]	[at %]
aCH-0	0.70	0	0.11	0.87	78.8	19.5
aCH-2	1.49	0	0.27	1.50	80.6	16.1
aCH-4	0.40	0	0.10	0.50	78.8	20.2
aCH-6	0.28	0	0.09	0.38	78.8	20.5
aCH-8	0.06	0	0.24	0.29	79.1	20.4
aCH-10	0.05	0.09	0.25	0.36	79.9	19.4

Figure 4.3 shows the depth profiles of the H-content in all deposited films. The depth resolution for H with about 80 nm is worse than for the other elements because different detection systems had to be used. Therefore, the profile only slowly reaches

its maximum. The poor depth resolution might also explain the decrease of the H concentration with increasing depth.

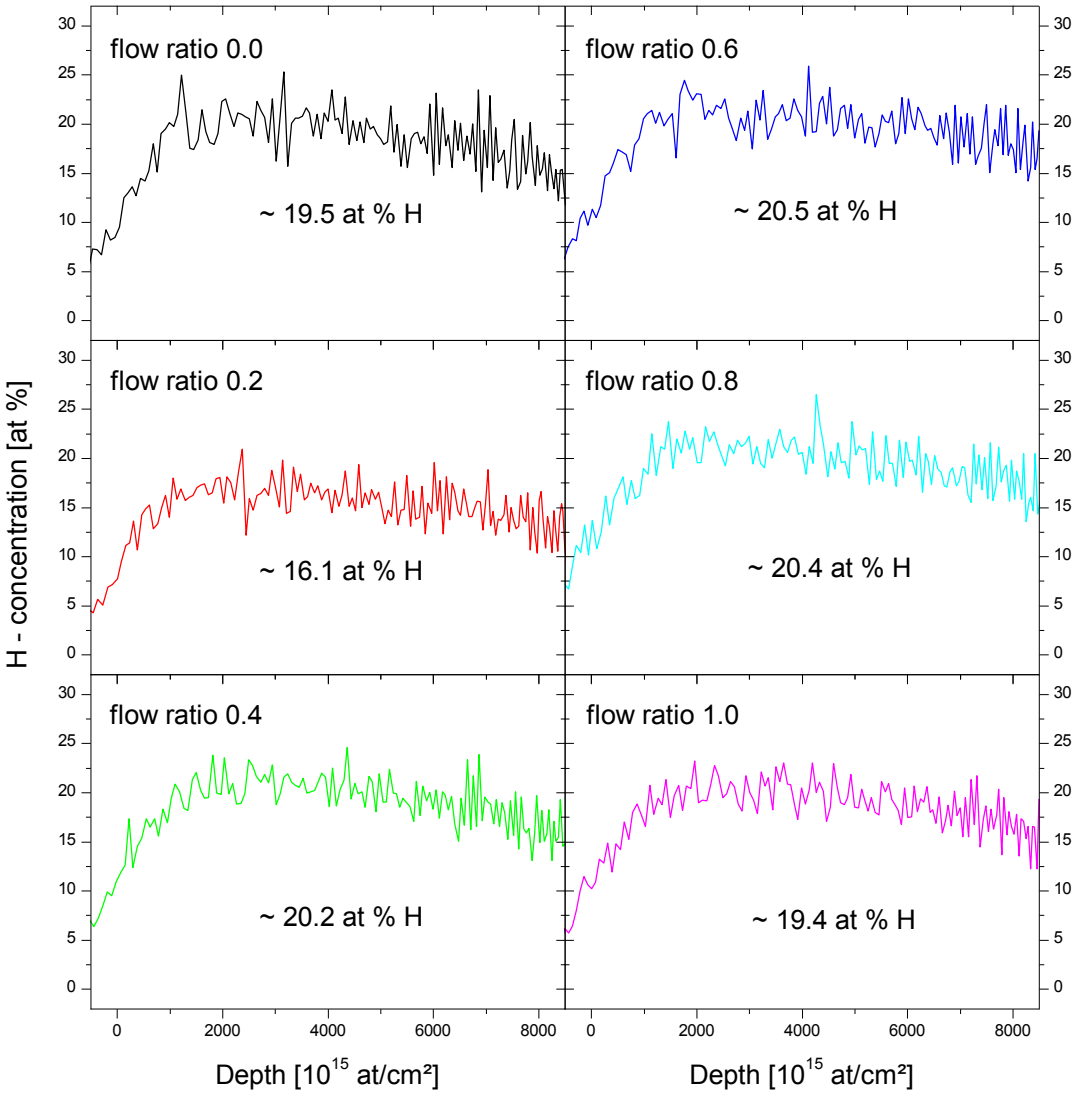

Figure 4.3: ERDA depth profiles of the H-content for the deposited a-C:H films with different C_2H_2/Ar flow ratios.

4.3 X-Ray Diffraction

The XRD patterns (Figure 4.4) confirm the expected amorphous structure of the film. It should be noted that the typical graphite peak would appear at about 26° [31]. The sharp peak at about 53° originates from the Si-substrate [31] and the small peak beside results from a slightly tilted angle of incidence. The elevated background at $2\theta < 20°$ is most probably related to the amorphous film structure and to a partial reflection of the X-ray beam at low detector angles.

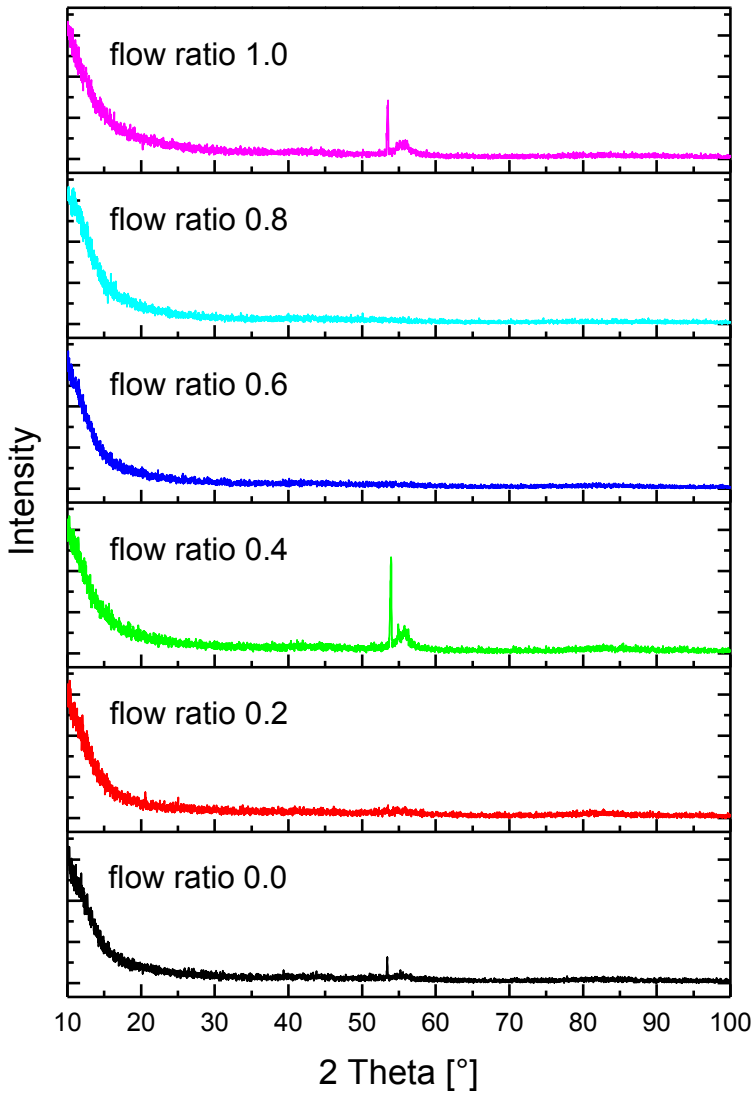

Figure 4.4: XRD patterns of the amorphous carbon films grown on Si substrates with various C_2H_2/Ar flow ratios.

4.4 X-Ray Photoelectron Spectroscopy

The samples were measured as received, without heating process or sputter cleaning to avoid damaging of the chemical bonds. Figure 4.5 shows an exemplary XPS general survey scan of an a-C:H film. It provides information about the present elements in the coating. In this case only carbon (C 1s peak) and negligible oxygen (O 1s peak) were detected. The oxygen might arise from adsorbed water or oxygen picked up during storage at ambient atmosphere [32]. For fitting the C 1s peak at 285 eV, the software UniFit with the Powell fitting algorithm was used to estimate the sp^2 and sp^3 fraction.

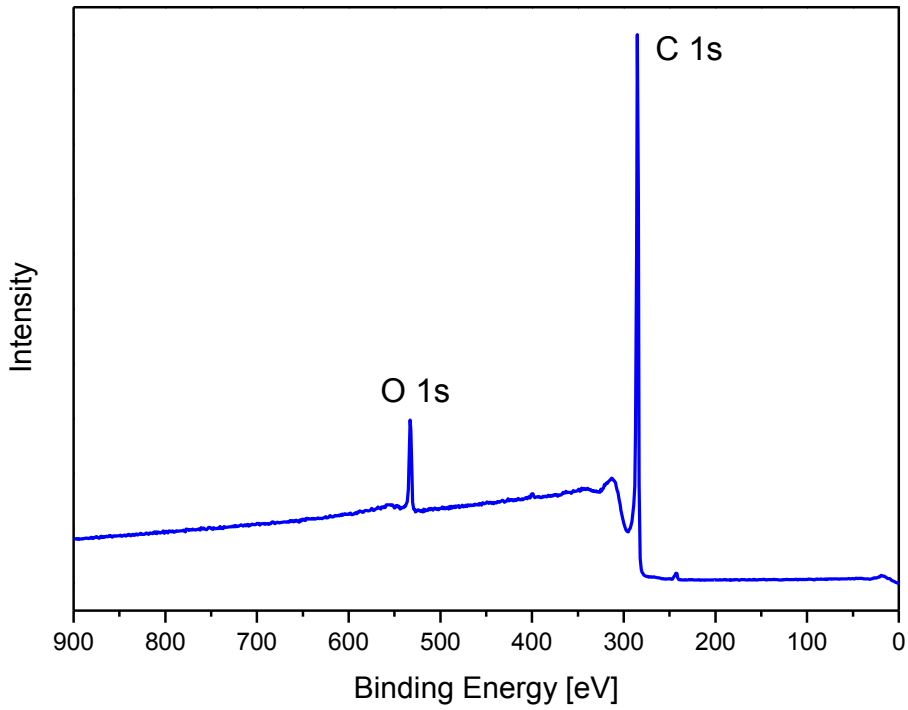

Figure 4.5: A representative wide XPS scan spectrum showing the oxygen 1s and carbon 1s orbital (sample aCH-0).

Figure 4.6 compares the fitted XPS spectra for all coatings. The sp^2 peak was found at 284.5 and the sp^3 peak at 285.5 eV, which fits well to literature. There, the sp^2 peak shows up at 284.4 and the sp^3 peak at 285.2 eV [6] [33]. The shoulder from 286 to 290 eV is due to surface contamination during storage at ambient atmosphere.

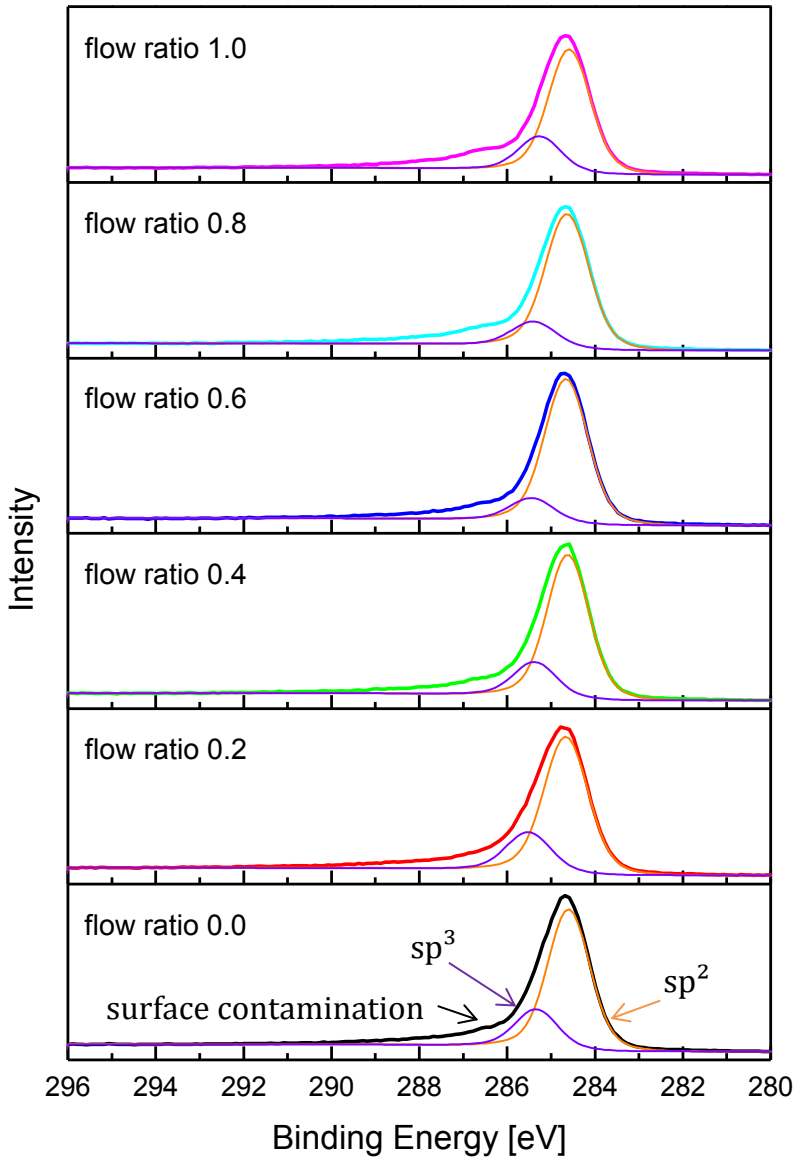

Figure 4.6: Fitted XPS spectra of the C 1s peak showing the sp^2 and sp^3 fraction as well as surface contamination.

4.5 Raman Spectroscopy

Figure 4.7 (a) shows a Raman spectrum of an amorphous carbon film deposited in pure Ar atmosphere with the Gaussian fits for the D- and G-band. All measured films are characterised by a highly disordered carbon phase. The D-band was found at about 1380 cm^{-1} and the G-band at about 1560 cm^{-1}. In literature, the positions are given at 1360 and 1560 cm^{-1} [16] [34], which fits well.

Compared to literature (Figure 4.7 (b), [35]), the shape of the Raman spectra and the band parameters rather show up an a-C:H structure instead of an a-C structure even if the film is deposited with Ar as sputtering gas only [30]. This can be explained by a relatively high ion energy level because of a low distance between target and substrate [36]. Due to the lower distance, a more intense Ar^+ bombardment can be assumed and the film is more disordered.

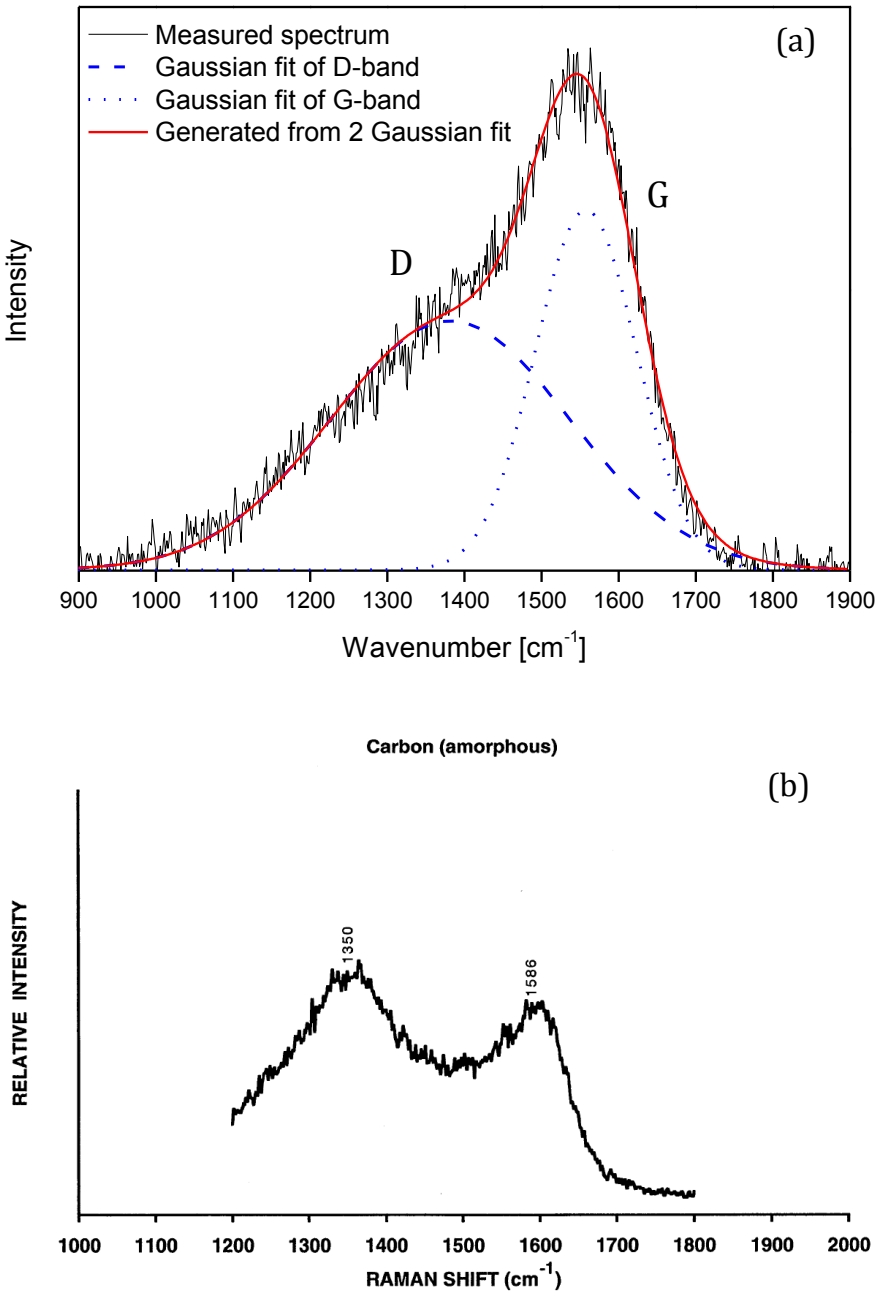

Figure 4.7: Raman spectrum of (a) a measured amorphous carbon film deposited without reactive gas compared to (b) an amorphous carbon film as reported in [35].

Figure 4.8 compares the deposited films concerning the fitted D- and G-band. It can be observed, that the height of the G-band increases with the C_2H_2/Ar flow ratio. Furthermore, the G-band slightly moves to higher wavenumbers, simultaneously the D-band moves to lower wavenumbers. In literature, it is mentioned that the clustering of the sp^2 phase mainly affects the peak positions, width and intensity [37]. In principle, the sp^2 clustering can vary independently from the sp^3 content. That means for a given sp^3 content and excitation energy, a number of different Raman spectra, or, equivalently, similar Raman spectra for different sp^3 contents are possible [37].

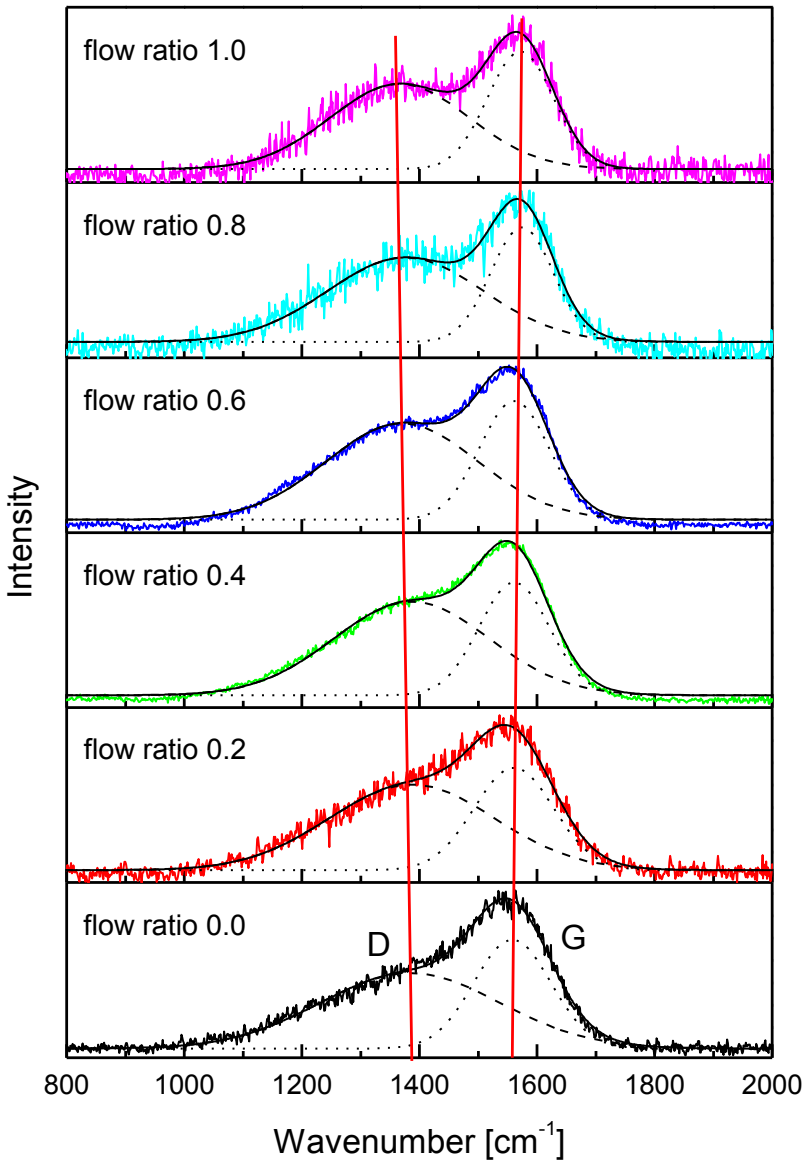

Figure 4.8: Raman spectra of the a-C:H films deposited with different C_2H_2/Ar flow ratios.

The interpretation of Raman spectra is quite complex, therefore some guidelines should be noted [16] [38] [34] [39]:

- The G-band of the Raman spectrum taken at visible excitation has its origin in the effect of bond stretching of all carbon atoms in sp^2 hybridisations, both in rings and chains.
- The D-band occurs from the breathing mode of carbon atom rings.
- The ID/IG – ratio is an indicator for the sp2 phase organised in rings. A low or nearly zero value of the ID/IG – ratio suggests an sp2 phase organised in chains, whereas a high ID/IG – ratio is a sign of increasing sp2 aromatic rings.
- In the case of a-C:H films, the sp3-hybridisated carbon fraction can be estimated by the Raman parameters. A higher comprehensive (C-C, C-H) sp3 content is related to a low ID/IG – ratio.
- The FWHM (G) is used in order to show the trends in the C-C sp3 bonding content. If the FWHM (G) increases in equal measure, the C-C sp3 bonding content increases.

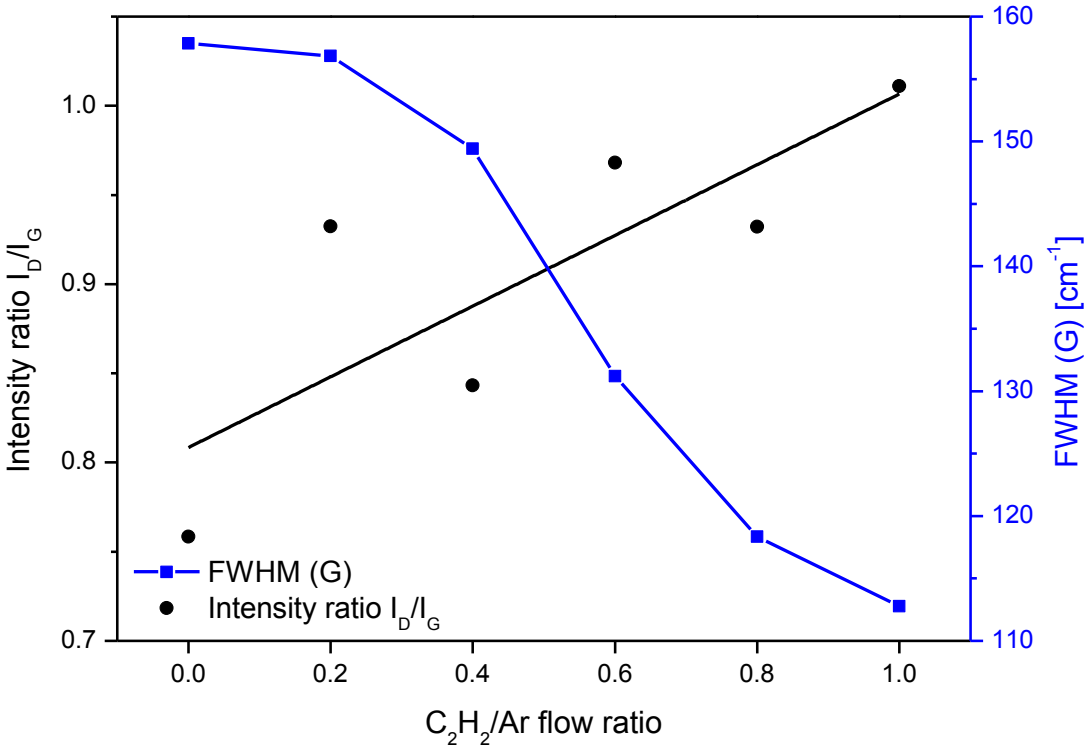

Figure 4.9: Intensity ratio I_D/I_G and FWHM (G) as a function of the C_2H_2/Ar flow ratio of the deposited films.

Compared to these guidelines, Figure 4.9 can be interpreted as follows: with increasing sp^3 content, the intensity ratio I_D/I_G increases due to an increasing amount of graphitic rings, while FWHM (G) decreases due to a more ordered structure [40].

Figure 4.10 shows an in situ Raman measurement of the deposited films from room temperature up to 300°C. It can be observed that in general the I_D/I_G ratio increases for all samples. Equally with increasing flow ratio the I_D/I_G ratio increases. Simultaneously, FWHM (G) decreases with increasing temperature and with increasing flow ratio the general values of FWHM (G) decrease. Amorphous carbon is known to have a phase transformation above 150°C due to bonded hydrogen liberation [41] [30], which results in increasing size of graphite clusters and affects the I_D/I_G ratio and FWHM (G).

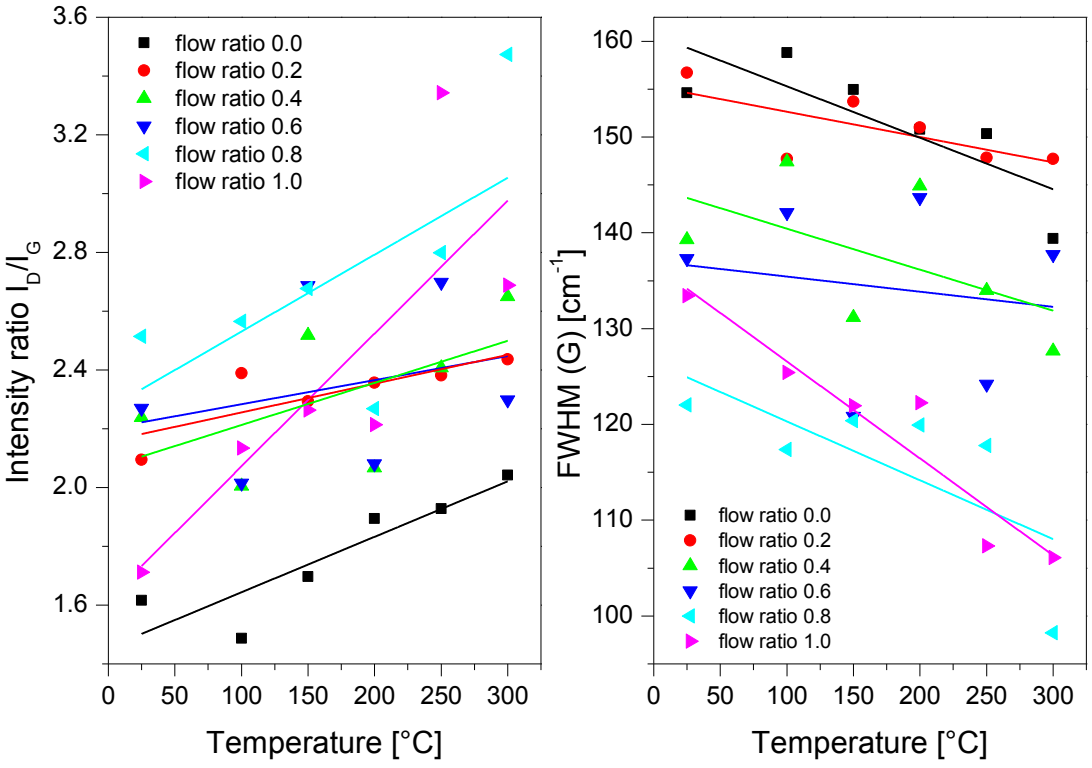

Figure 4.10: In-situ Raman measurements for all deposited films showing the temperature-dependence of the I_D/I_G ratio and FWHM (G).

4.6 Nanoindentation

The measured hardness and Young's modulus of the deposited films are shown in Figure 4.11 as a function of the C_2H_2/Ar flow ratio. For C_2H_2/Ar flow ratios above 0.2, the hardness continuously decreases from 25 to 8 GPa and the Young's modulus decreases from about 187 to 55 GPa, respectively. In literature the hardness varies between 10 and 20 GPa for typical a-C:H films with a H-content between 30 and 40 at % [6]. The decrease of the mechanical properties with increasing C_2H_2/Ar flow ratios is related to a more disordered or even polymeric structure.

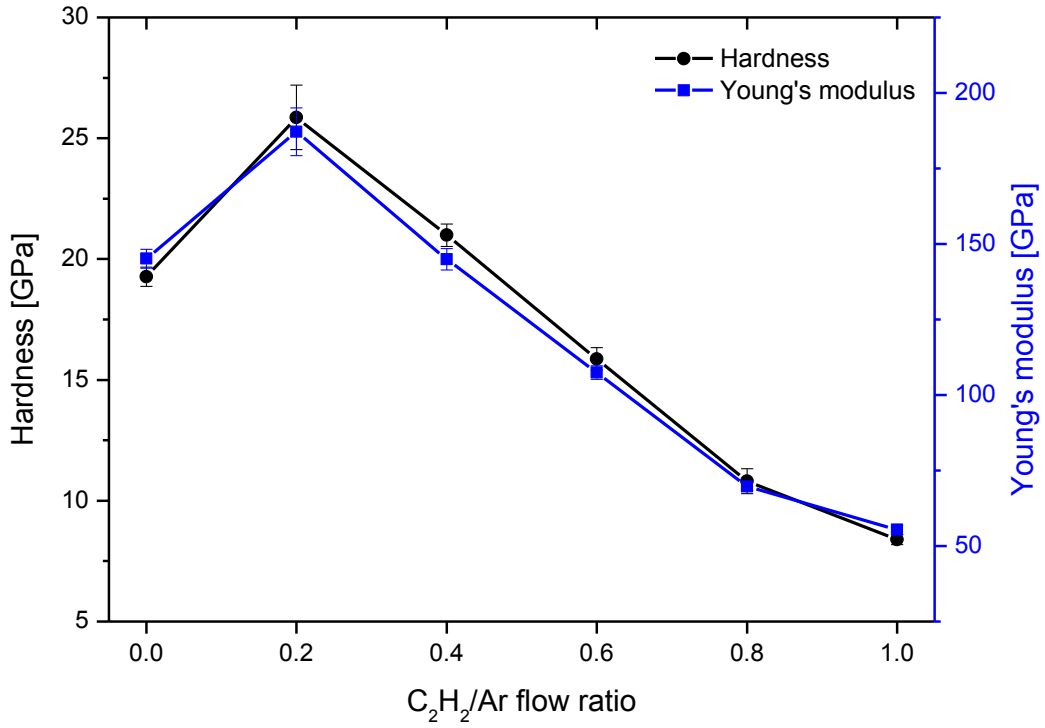

Figure 4.11: Hardness and Young's modulus of the deposited coatings as a function of C_2H_2/Ar flow ratio.

4.7 Residual Stresses

Figure 4.12 shows a schematic curve of the residual stress in a coating versus temperature. From point 1 to 2, the curve indicates a thermo-elastic behaviour with a low slope due to the similar thermal expansion coefficients α of the Si-substrate and the a-C:H coating (Si: 2.6×10^{-6} K^{-1} [42], graphite: $1.9 - 2.9 \times 10^{-6}$ K^{-1} [43]). Point 2 corresponds to the deposition temperature T_d. Therefore, a radical change of the

slope would be expected after this point due to structural rearrangements, like healing of point defects. At point 3, which corresponds to the critical temperature T_{cr}, there is a knee which indicates more dramatic structural changes. For the a-C:H films, there can be a hydrogen liberation or even a transformation from sp^3 to sp^2. The course of the curve from point 4 to 5 shows a well relaxed behaviour, which is again characterised by thermo-elasticity.

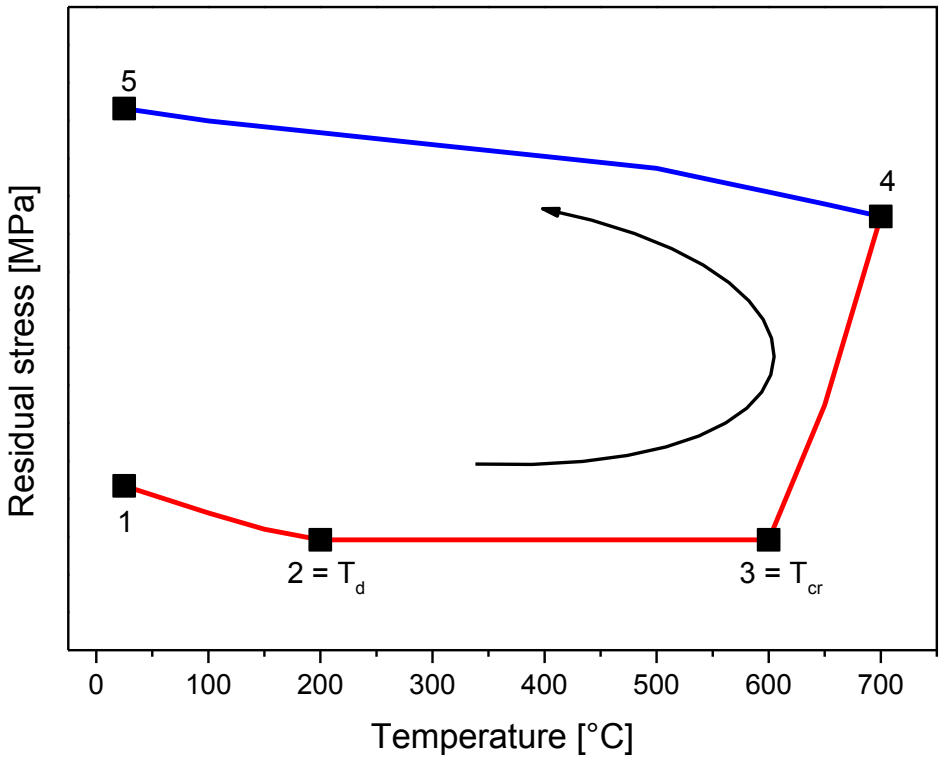

Figure 4.12: Schematic curve shape of a residual stress measurement versus temperature showing the key points.

In Figure 4.13, the different coatings are compared concerning the residual stresses during a heating and cooling process. In general, all deposited coatings have stresses that are compressive in nature. It can be observed that the mentioned critical temperature T_{cr} slightly increases from 550 to 650°C for the coatings with an C_2H_2/Ar flow ratio from 0.0 to 0.6. The samples grown with flow ratios of 0.8 and 1.0 show an obvious decrease of the critical temperature to 350°C. Furthermore, also the stresses in the as-deposited condition are significantly lower than in those grown at lower flow ratios. These coatings grown at high flow ratios are characterised by a

fully relaxed behaviour after cooling, which corroborates their polymeric behaviour. This could be related to the observed more pronounced graphitic structure, as already mentioned in section 4.5.

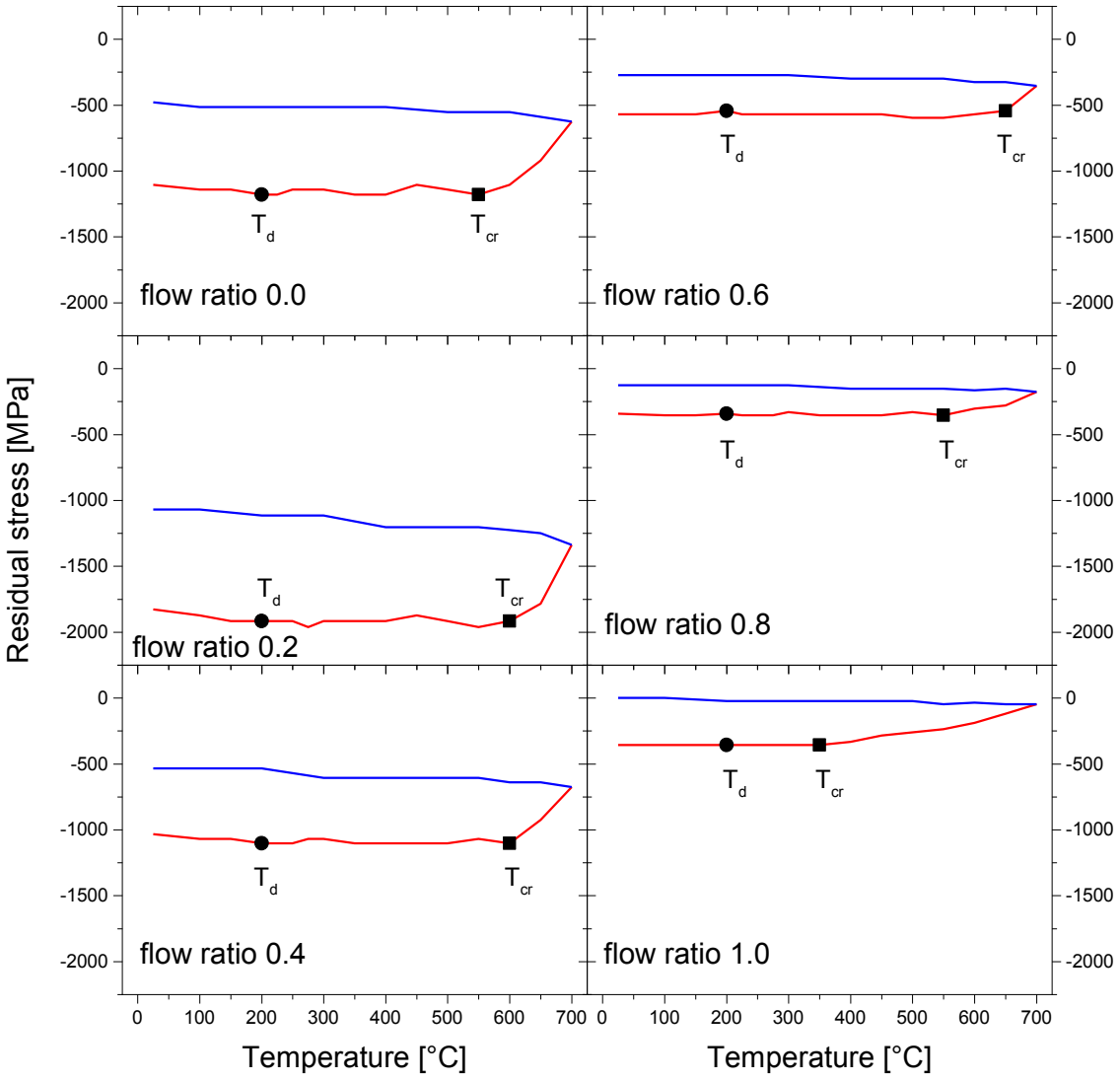

Figure 4.13: Coating stress as a function of temperature for the coatings deposited using different C_2H_2/Ar flow ratios (red: heating, blue: cooling).

5 Discussion

5.1 Correlation between structural and mechanical properties

Figure 5.1 demonstrates a comparison of the structural information obtained from Raman spectroscopy and the mechanical properties of the coatings. The FWHM (G) is direct proportional to the mechanical properties, like hardness and Young's modulus and indirect proportional to the intensity ratio I_D/I_G [39]. Therefore, elevated C_2H_2 concentrations in the process gas atmosphere induce an ordering effect in the films as well as a higher degree of polymerisation, which results in a decrease of hardness and Young's modulus [40].

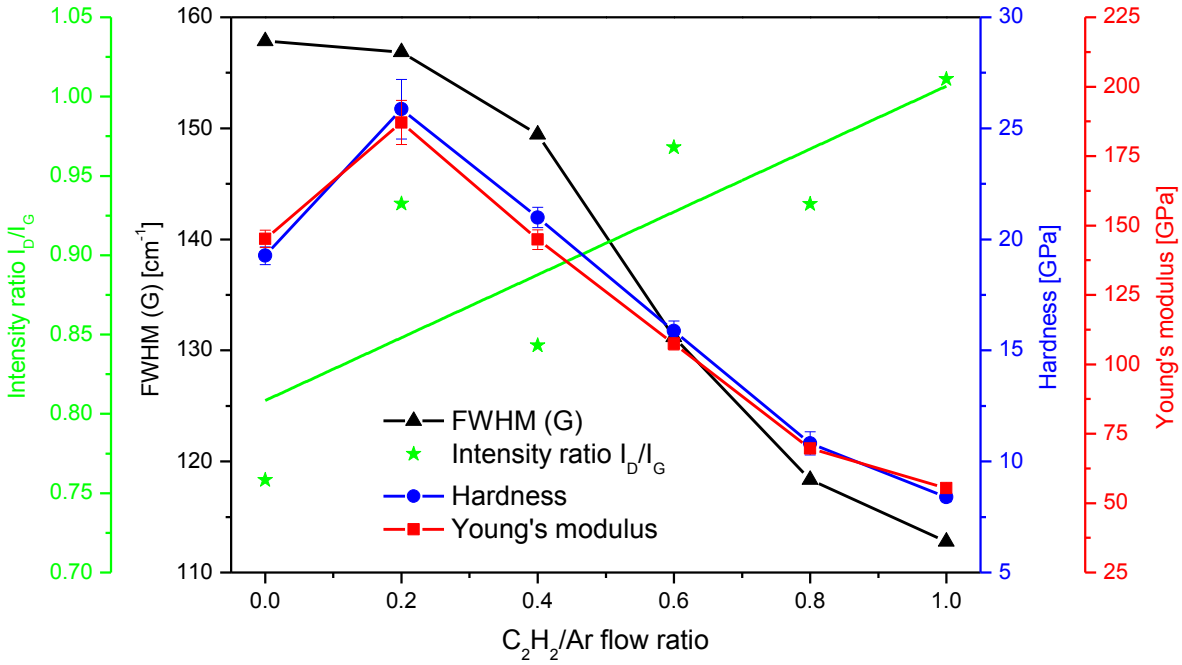

Figure 5.1: Comparison of structural information with mechanical properties of the deposited a-C:H films as a function of the C_2H_2/Ar flow ratio.

5.2 Correlation between deposition gas mixture and hydrogen content

As shown in section 4.2, the ERDA measurements yielded an average H-content of about 20 at % for all deposited films. However, due to the variation of the C_2H_2/Ar flow ratio also a varying H-content would have been expected. Thus, although no

unambiguous answer to this question can be offered within this thesis, some reasons for the nearly unaffected H-content are discussed in the following:

- First of all, a leak in the overall condition of the deposition system could be expected. An indication for this would be a high content of oxygen in the coatings. However, from the results of the ERDA measurements this factor can be excluded, since the average oxygen contamination was below 1 at %.
- A further reason could be a leak within the C_2H_2 mass flow controller, i.e. where the valve does not open and close exactly. Therefore, the possibility could exist that either no or not enough C_2H_2 is added to the deposition gas mixture or that the valve does not close after deposition and additional C_2H_2 might react with the still hot coating. However, it has to be noted, that the brightness and coloration of the plasma intensified with increasing C_2H_2/Ar flow ratio. The total pressure during deposition increased from 8×10^{-3} to above 2×10^{-2} mbar (see Table 3.1) and also the film growth rate increased (see Figure 4.2). Altogether, this indicates an increasing C_2H_2 content in the deposition gas mixture, since the other deposition parameters like power supply or bias voltage were kept constant. Moreover, the residual pressure of about 4×10^{-6} mbar after deposition speaks against a leak within the mass flow controller.
- The carbon target could have adsorbed water or oxygen out of the atmosphere due to a long storage. However, this would also result in a high contamination of oxygen. Since the target was new and the contamination is below 1 at %, this fact can be excluded as well.
- The deposited samples could absorb water or oxygen out of the atmosphere during storage. However, also in this case a higher content of oxygen would appear in the ERDA results.
- As a last point, which has to be considered, although the mass flow controller was immediately closed at the end of deposition, there could be a residual H-content within the gas background. This is fostered by the fact that hydrogen is the lightest element, which results in the lowest pumping efficiency of the turbomolecular pump [44]. Furthermore, Schneider et al. [45] also explained this phenomenon of hydrogen uptake in amorphous alumina thin films resulting from the high vacuum gas background.

Concluding, it has to be said that further investigations or even recurring deposition runs have to be done to unambiguously clarify the missing correlation between C_2H_2/Ar flow ratio and H-content.

6 CONCLUSION AND OUTLOOK

6.1 Conclusion

Within this work, hydrogen containing diamond-like carbon coatings were synthesised by reactive unbalanced magnetron sputtering in an argon/acetylene (Ar/C_2H_2) atmosphere with C_2H_2/Ar flow ratios increasing from 0 to 1. The aim was to contribute to the design of biocompatible coatings for medical implants based on magnesium with high H-content and a polymeric structure, to be used as a diffusion barrier between the implant and the surrounding tissue.

The deposited coatings were studied concerning their composition, structure and mechanical properties. The coating thickness varied between 1.4 (without C_2H_2) and 2.2 µm (C_2H_2/Ar flow ratio of 1.0). ERDA measurements yielded an average H-content of about 20 at % and contaminations of oxygen and nitrogen below 1 at %. XRD measurements confirmed the expected amorphous structure of the films. With XPS and Raman spectroscopy the sp^2 and sp^3 fractions were determined, which are directly related to the intensity ratio I_D/I_G. With increasing I_D/I_G ratio, the coating structure got more disordered. With an increasing C_2H_2/Ar flow ratio, the hardness decreased from 25 to 8 GPa and the Young's modulus from 187 to 55 GPa, which indicates an increasing polymeric film structure as well. The residual stress measurements showed compressive stresses for all coatings with different critical temperatures for defect healing processes.

6.2 Outlook

This thesis contributes towards the framework conditions for synthesising hydrogenated amorphous carbon films for medical applications. With elevated C_2H_2-content, films with even polymeric behaviour can be synthesised. Some ideas for future developments on these films are: To illuminate the bonding structure further, Raman spectroscopy measurements with different wavelengths could be done. Furthermore, transmission electron microscopy (TEM) measurements could give information about the C-H bonding. Next to structural investigations, the a-C:H films could be deposited on magnesium substrates to study the interaction between film and substrate.

On the basis of this diploma thesis, the functionality of the coating system could be further improved. Forward-looking, the amorphous carbon diffusion barrier should on the one hand prevent a temporary magnesium implant from corrosion during a fracture healing process. On the other hand, a slow degradation of the film should ensure a controlled access of water to the magnesium surface due to a specific porosity and for controlled wear of the film. This should provide a controlled degradation of the implant. Next to the corrosion properties, antibacterial additives like silver could be built into the near-surface zone of the coating to avoid an inflammation of the surrounding tissue in the first days after surgery. Moreover, tests in biological solutions (in vitro) and living organism (in vivo) need to be done to further proof the biocompatibility of films based on this concept.

REFERENCES

[1] F. Witte, The history of biodegradable magnesium implants: A review, Acta Biomaterialia 6, 2010, pp. 1680-1692.

[2] F. Witte, V. Kaese, H. Haferkamp, E. Switzer, A. Meyer-Lindenberg, C. J. Wirth and H. Windhagen, In vivo corrosion of four magnesium alloys and the associated bone response, Biomaterials 26, 2005, pp. 3557-3563.

[3] http://en.wikipedia.org/wiki/File:Eight_Allotropes_of_Carbon.png, 2013.

[4] J. Robertson, Amorphous carbon, Advances in Physics 35, 1986, pp. 317-374.

[5] S. Ravi and P. Silva, Properties of Amorphous Carbon, London: INSPEC, 2003.

[6] J. Robertson, Diamond-like amorphous carbon, Materials Science and Engineering R37, 2002, pp. 129-281.

[7] W. Jacob and W. Möller, On the structure of thin hydrocarbon films, Applied Physics Letters 63, 1993, pp. 1771-1773.

[8] C. Donnet and A. Erdemir, Tribology of Diamond-Like Carbon Films, New York: Springer, 2008.

[9] F. Rovere, Theoretical and experimental assessment of Cr-Al-Y-N as protective coating for y-TiAl based alloys, PhD Thesis, Rheinisch-Westfälische Technische Hochschule, Aachen, 2009.

[10] R. D. Arnell and P. J. Kelly, Recent advances in magnetron sputtering, Surface and Coatings Technology 112, 1999, pp. 170-176.

[11] M. Ohring, The Material Science of Thin Films, San Diego: Academic Press, 2002.

[12] J. L. Vossen and W. Kern, Thin Film Processes II, Boston: Academic Press, 1991.

[13] R. A. Haefer, Oberflächen- und Dünnschicht-Technologie Teil I, Heidelberg: Springer, 1987.

[14] R. Singh, C. V. Raman and the discovery of the Raman effect, Physics in Perspective 4, 2002, pp. 399-420.

[15] http://en.wikipedia.org/wiki/raman_spectroscopy, 2013.

[16] A. C. Ferrari and J. Robertson, Interpretation of Raman spectra of disordered and amorphous carbon, Physical Review B61, 2000.

[17] A. C. Ferrari, B. Kleinsorge, G. Adamopolous, J. Robertson, W. I. Milne, V. Stolojan, L. M. Brown, A. LiBassi and B. K. Tanner, Determination of bonding in amorphous carbons by electron energy loss spectroscopy, Raman scattering and x-ray reflectivity, Journal of Non-Crystal Solids 266-269, 2000, pp. 765-768.

[18] User Manual Z 400, Leybold AG.

[19] User Guide Tylan General R 7030/7031, Tylan General GmbH.

[20] User Manual Duo 2, Pfeiffer Vacuum GmbH, 2002.

[21] User Guide Leybold Vacuum, Leybold AG.

[22] L. Ecuyer, C. Brassard, C. Cardinal and J. Chabball, An accurate and sensitive method for the determination of the depth distribution of light elements in heavy materials, Journal of Applied Physics 47, 1976, pp. 381-382.

[23] J. Tirira and P. Trocellier, Elastic recoil detection analysis: theoretical analysis of scattering cross section and basic parameters, Journal of Radioanalytical and Nuclear Chemistry 130, 1989, pp. 311-319.

[24] A. C. Fischer-Cripps, Nanoindentation, New York: Springer, 2004.

[25] A. Cavaleiro and J. T. M. De Hosson, Nanostructured Coatings, New York: Springer, 2006.

[26] W. C. Oliver and G. M. Pharr, An improved technique for determining hardness and elastic modulus using load an displacement sensing indentation experiments, Journal of Materials Research 7, 1992, pp. 1564-1583.

[27] D. Winkler, Konzeption und Realisierung eines thermisch unterstützten Messverfahrens zur Bestimmung von Eigenspannungen in dünnen Schichten, Master's thesis, Montanuniversität, Leoben, 1997.

[28] M. Rubin, C. B. Hopper, N.-H. Cho and B. Bhushan, Optical and mechanical properties of d.c. sputtered carbon films, Journal of Materials Research Volume 5, 1990, pp. 2538-2542.

[29] J. Schwan, S. R. P. Silva, J. Robertson, S. Ulrich, H. Roth, H. Ehrhardt, R. Samlenski and R. Brenn, Tetrahedral amorphous carbon films prepared by magnetron sputtering and dc ion plating, Journal of Applied Physics 79, 1996, pp. 1416-1422.

[30] M. Kahn, Room-temperature deposition of DLC films by an ion beam method, reactive magnetron sputtering and pulsed laser deposition: process design, film structure and film properties, PhD-Thesis, Montanuniversität, Leoben, 2009.

[31] Powder diffraction files, (card 00-056-0159 for graphite and card 00-027-1402 for silicon), International Centre for Diffraction Data, ICDD-JCPDS, 2007.

[32] J. Filik, P. W. May, S. R. J. Pearce, R. K. Wild and K. R. Hallam, XPS and laser Raman analysis of hydrogenated amorphous carbon films, Diamond & Related Materials 12, 2003, pp. 974-978.

[33] P. Mérel, M. Tabbal, M. Chaker, S. Moisa and J. Margot, Direct evaluation of the sp^3 content in diamond-like-carbon films by XPS, Applied Surface Science 136, 1998, pp. 105-110.

[34] A. C. Ferrari and J. Robertson, Resonant raman spectroscopy of disordered, amorphous, and diamondlike carbon, Physikal Review B 64, 2001.

[35] J. S. Zabinski and N. T. McDevitt, Raman spectra of inorganic compounds related to solid state tribochemical studies, Ohio: Materials Directorate, Wright Laboratory, 1996.

[36] J. Robertson, Mechanism of sp^3 bond formation in the growth of diamond-like carbon, Diamond & Related Materials 14, 2005, pp. 942-948.

[37] C. Casiraghi, F. Piazza, A. C. Ferrari, D. Grambole and J. Robertson, Bonding in hydrogenated diamond-like carbon by Raman spectroscopy, Diamond & Related Materials 14, 2005, pp. 1098-1102.

[38] A. C. Ferrari and J. Robertson, Raman spectroscopy of amorphous, nanostructured, diamond-like carbon, and nanodiamond, Philosophical Transactions of the Royal Society A 362, 2004, pp. 2471-2512.

[39] C. Casiraghi, A. C. Ferrari and J. Robertson, Raman spectroscopy of hydrogenated amorphous carbons, Physical Review B 72, 2005.

[40] M. Kahn, M. Čekada, R. Schöberl, H. Parizek, B. Raninger, R. Berghauser, W. Waldhauser and E. Brandstätter, DLC films deposited at room temperature by reactive magnetron sputtering and by an anode layer source - a comperative study, Proceedings of the 17th Plansee Seminar Vol 2 HM 40/1, 2009.

[41] G. Gassner, P. H. Mayrhofer, J. Patscheider and C. Mitterer, Thermal stability of nanocomposite CrC/a-C:H thin films prepared by magnetron sputtering, Thin Solid Films, 2007, pp. 5411-5417.

[42] W. M. Haynes, CRC Handbook of Chemistry and Physics, London: Taylor & Francis, 2011.

[43] W. Martienssen and H. Warlimont, Springer Handbook of Condensed Matter and Material Data, Berlin: Springer, 2005.

[44] C. Edelmann, Vakuumtechnik, Heidelberg: Hüthig, 1986.

[45] J. M. Schneider, A. Anders, B. Hjörvarsson, I. Petrov, K. Macák, U. Helmersson and J. Sundgren, Hydrogen uptake in alumina thin films synthesized from an aluminum plasma stream in an oxygen ambient, Applied Physics Letters 74, 1999, pp. 200-202.

[46] M. Kahn, W. Waldhauser, C. Mitterer, T. Koch, A. Pauschitz, E. Brandstätter and M. Roy, Nanoindentation and nanoscratch behaviour of room-temperature reactive pulsed magnetron sputtered DLC films-correlations with film structure, submitted.

[47] A. C. Ferrari, A. Libassi, B. K. Tanner, V. Stolojan, J. B. L. M. Yuan, S. E. Rodil, B. Kleinsorge and J. Robertson, Density, sp^3 fraction, and cross-sectional structure of amorphous carbon films determined by x-ray reflectivity and electron energy-loss spectroscopy, Physical Review B62, 2000.